Noble gases in shocked igneous rocks from the 380 Ma-old Siljan impact structure (Sweden): A search for paleo-atmospheric signatures

Fanny Cattani, Guillaume Avice, Ludovic Ferrière, Sanna Alwmark

Chemical Geology xxx (xxxx) 122440

Contents lists available at ScienceDirect

Chemical Geology

journal homepage: www.elsevier.com/locate/chemgeo

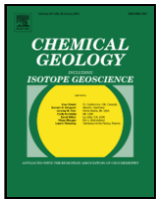

Noble gases in shocked igneous rocks from the 380 Ma-old Siljan impact structure (Sweden): A search for paleo-atmospheric signatures

Fanny Cattani [a,*], Guillaume Avice [a], Ludovic Ferrière [b,c], Sanna Alwmark [d]

[a] Université Paris Cité, Institut de Physique du Globe de Paris, CNRS, F-75005 Paris, France
[b] Natural History Museum Abu Dhabi, Saadiyat Island, Abu Dhabi, United Arab Emirates
[c] Natural History Museum Vienna, Burgring 7, A-1010 Vienna, Austria
[d] Department of Geology, Lund University, Sölvegatan 12, 223 62 Lund, Sweden

ARTICLE INFO

Editor: Don Porcelli

Keywords:
Geochemistry
Noble gases
Impact crater
Shocked quartz
Paleo-atmosphere
Fluid inclusion

ABSTRACT

Finding direct records of the ancient Earth's atmosphere is key to understand the evolution of the entire planet. Nevertheless, such records are scarce, and only a few geological samples with preserved paleo-atmospheric signatures are available today. In this study, we analyzed noble gases contained in shocked granitic and volcanic rocks collected across the 380 Ma-old Siljan impact structure (in Sweden) to investigate the potential of shocked quartz crystals with planar deformation features (PDFs), often decorated by fluid inclusions, to preserve atmospheric signatures.

Our results reveal that most of the investigated samples show relative elemental abundances of noble gases falling between those of air and meteoric water values. Atmospheric gases are present in the samples but excesses in radiogenic, nucleogenic, and fissiogenic noble gas isotopes highlight interactions of fluids with crustal rocks during the impact-generated hydrothermal circulation of fluids after the impact. Such fluid circulation event(s) could also have remobilized older fluids originally present in fluid inclusions preserved in the mineral lattices. Furthermore, results obtained on the two pure quartz fractions highlight a stronger atmospheric signature correlated with the presence of PDFs. The atmospheric component detected in this study could represent either a paleo-atmospheric signature trapped shortly after the Siljan impact event, or it may result from modern atmospheric contamination. Future studies of noble gases contained within shocked quartz crystals from other impact structures will unveil if such samples present advantages compared to other paleo-atmospheric proxies.

1. Introduction

The composition of the Earth's atmosphere is controlled by various bio-chemical and physical processes, such as biological activity, magma outgassing, impact events, atmospheric escape, subduction, etc. All these processes have varied with time leading to changes in the elemental abundance and isotopic composition of volatile elements in the Earth's atmosphere (Catling and Kasting, 2017; Catling and Zahnle, 2020). Studying atmospheric evolution allows to improve our knowledge of the geological history of our planet and its potential for sustaining life. Especially, understanding the evolution of the ancient atmosphere is crucial to define the parameters controlling the atmospheric escape and the contribution of the volatile elements from impact events that were most important on the early Earth (Catling and Kasting, 2017; Ehlmann et al., 2016).

The elemental abundances and isotopic composition of noble gases represent an integrated archive of the evolution of the planet. Noble gases represent about 1 % of the Earth's modern atmosphere and are chemically inert, inducing a long residence time in the atmosphere. Additionally, radiogenic noble gases are reliable chronometers and can be used to date the important processes behind planetary evolution. Hence, noble gases can be used as tracers of the multiple physical and geological processes that shaped the Earth's atmosphere, and studying their elemental abundances and isotopic compositions provides critical information about the evolution of the planetary atmospheres (Burnard, 2013; Catling and Kasting, 2017; Marty, 2020; Ozima and Podosek, 2002; Porcelli and Ballentine, 2002).

Recent studies indicate that only few geological samples have recorded information about the composition of the ancient atmosphere (e.g., Almayrac et al., 2021; Avice et al., 2018; Avice et al., 2017; Blamey et al., 2016; Pujol et al., 2011) Indeed, analyses of volatile ele-

* Corresponding author at: Institut de physique du globe de Paris, CNRS, F-75005 Paris, France.
E-mail address: cattani@ipgp.fr (F. Cattani).

https://doi.org/10.1016/j.chemgeo.2024.122440
Received 17 June 2024; Received in revised form 23 September 2024; Accepted 2 October 2024
0009-2541/

ments trapped in fluid inclusions contained in hydrothermal minerals (such as quartz, barites, halites) collected from Archean cratons and Proterozoic deposits (between 3.5 Ga and 400 Ma) identify the presence of paleo-atmospheric noble gas end-members mixed with crustal gases carrying nucleogenic, radiogenic, and fissiogenic excesses. Determining the elemental and isotopic composition of the paleo-atmospheric end-member provides constraints on processes that have shaped our atmosphere, such as the geodynamic and temporal evolution of the Earth's reservoirs (e.g., Almayrac et al., 2021; Avice et al., 2018; Blamey et al., 2016; Pujol et al., 2011). Nevertheless, several challenges associated with conventional paleo-atmospheric proxies persist. These issues include the preponderant excess of radiogenic ^{40}Ar (^{40}Ar*), the influence of crustal components, the low amounts of gases contained in the samples, the lack of precise geochronological data regarding sample formation, and the complexity of samples' formation and preservation history potentially affected by multiple geological events such as late hydrothermal overprint (e.g., Avice et al., 2018; Avice et al., 2017; Bekaert et al., 2018). Therefore, a major goal of paleo-atmospheric studies involves identifying new reliable and datable proxies. A geological sample can be considered as a valuable paleo-atmospheric proxy when it contains a well-preserved and measurable atmospheric signal, and if an age can be confidently assigned to this atmospheric signal (Avice et al., 2023).

This study aimed to uncover new paleo-atmospheric proxies by examining unique geological contexts, such as impact craters. Impact craters present significant advantages due to the extensive geological knowledge on them and knowing that they are formed very quickly, and for some of them their formation age is well-established (e.g., Osinski et al., 2022; Schmieder and Kring, 2020). Additionally, a large number of impact craters are associated with post-impact hydrothermal circulation systems (e.g., Ames et al., 1998; Komor et al., 1988; Naumov, 2002; Newsom, 1980) characterized by hydrothermal minerals with a retrograde sequence of alteration minerals (Naumov, 2005). Moreover, impact-generated hydrothermal systems are relatively short-lived (i.e., in the case of very large impact structures, like the Chicxulub, it can be long live, in excess of 10^6 years; Kring et al., 2020) and relatively shallow as demonstrated by dating studies and modeling works (e.g., Abramov and Kring, 2007; Ames et al., 1998; Naumov, 2002). Consequently, these systems are likely to be dominated by air-saturated waters, which facilitates their characterization compared to more conventional hydrothermal veins (Naumov, 2002). Hence, geological samples found in impact structures are interesting targets for paleo-atmospheric studies because, if a paleo-atmospheric signal was introduced at the time of the impact or shortly thereafter, they could represent well-dated snapshots of the composition of the atmosphere. A feasibility study on samples from the Rochechouart impact structure recently demonstrated that post-impact hydrothermal minerals preserve the signature of the ancient 200 Myr-old atmosphere with limited post-entrapment modifications (Avice et al., 2023). Hence, post-impact hydrothermal minerals can be considered as new paleo-atmospheric proxies.

In this study, we aimed to further investigate the potential of samples from impact craters by exploring the potential of shocked quartz grains as new paleo-atmospheric proxies. Contrary to hydrothermal quartz deposited in fractures and already explored successfully by Avice et al. (2023), shocked quartz grains are often magmatic in origin, with low initial amounts of trapped gases. Planar deformation features (PDFs), i.e., defining 'shocked quartz' form as the originally glassy planes (PDFs) recrystallize back to quartz and are often decorated by planar arrays of fluid inclusions (Goltrant et al., 1992; Trepmann and Spray, 2006) in all but the youngest impact structures on Earth. The question is: can we find a paleo-atmospheric component in fluid inclusions contained in shocked quartz grains? If yes, this would greatly enhance the number of geological samples available for paleo-atmospheric studies given the quasi-ubiquity of shocked quartz grains reported in impact crater setting. To test this idea, we conducted crushing experiments in order to measure the elemental abundances and isotopic composition of Ne, Ar, Kr, and Xe trapped in fluid inclusions contained in shocked quartz grains and whole rock samples from the 380 Ma-old Siljan impact structure (e.g., Jourdan et al., 2012). This approach enables us to track the origin of the fluid contained in fluid inclusions and to compare samples with PDFs with samples in which quartz is unshocked.

2. Samples and analytical method

2.1. Geological setting

The 380 Ma-old Siljan impact structure, located in Sweden, is the largest known impact structure in Western Europe (with a diameter between 52 and 75 km) (Jourdan et al., 2012). Studies carried out by Fredriksson and Wickman (1963) and Wickman et al. (1963) first identified the Siljan structure as a possible impact structure. It was then confirmed with the discovery of PDFs in quartz and shatter cones in the central part of the structure (Rondot, 1975; Svensson, 1973; Svensson, 1971; Tamminen and Wickman, 1980). The impact structure displays several structural units, including a central uplifted region surrounded by a ring-shaped depression (see e.g., Grieve, 1988; Grieve, 1982; Henkel and Aaro, 2005; Holm et al., 2011; Holm-Alwmark et al., 2017; Kenkmann et al., 2000). The central area, with a diameter of 28–30 km, is dominated by Dala granites of Järna and Siljan types, dating between 1.9 and 1.7 billion years (Herrmann et al., 2021) and belonging to the synorogenic Svecokarelian and post-Svecokarelian rock suites, respectively (Stephens, 2020). However, mafic intrusive, extrusive magmatic, and sedimentary rocks also occur sporadically within the structure. The study of PDFs in quartz from Siljan samples (e.g., Holm et al., 2011; Holm-Alwmark et al., 2017; Tamminen and Wickman, 1980) allows the estimation of shock pressures within the region of the central uplift. The lowest recorded pressures, ranging from 2 to 5 GPa, occur along the margin of the structure, while the highest pressure of ~20 GPa occurs at the center of the impact structure (Holm et al., 2011; Holm-Alwmark et al., 2017). In addition, there is generally a strong decoration of PDFs associated with "toasting" of quartz grains in samples located at the center of the structure (Short and Gold, 1996). This phenomenon is regarded as the result of either high densities of fluid inclusions predominantly located along decorated PDFs (Whitehead et al., 2002), and/or of vesiculation caused by pressure release at high post-shock temperatures (Ferrière et al., 2010). Several studies highlight that large impacts generate local hydrothermal systems driven by the impact melt sheet and uplifted basement heat sources (e.g., Ames et al., 1998; Komor et al., 1988; Naumov, 2002; Newsom, 1980; Newsom et al., 2001; Newsom et al., 1996). At Siljan, the existence of a post-impact hydrothermal system is attested by the identification of precipitated and altered hydrothermal mineral assemblages, such as hydrothermal Pb—Zn mineralization at the outer margin of the central uplift, or calcite crack-cements and intense chloritization of biotite in rocks from inside the central uplift (e.g., Herrmann et al., 2021; Johansson, 1984; Komor et al., 1988; Komor and Valley, 1990; Valley et al., 1988). Studies on fluid inclusions and altered minerals indicate a more intense fluid activity near the crater center, with trapping temperatures between 327 °C and 342 °C, that decreases toward outside the central uplift, with lower temperatures ranging from 40 °C to 225 °C (e.g., Drake et al., 2019; Herrmann et al., 2021; Hode et al., 2003; Komor et al., 1988). Furthermore, Komor et al. (1988) observed two fluid-inclusion populations at different depths, defined by different trapping temperatures, which may reflect distinct hydrothermal events: a deep Precambrian event (~1.7 Ga) active during the cooling of the Dala granites, and a shallow Devonian system (~380 Ma) driven by the heat of the impact melt sheet. This could explain why trapping temperatures at a given depth are higher than those predicted by extrapolating the gradients as-

sociated with the Precambrian event, and why there is a difference between the center and the rim of the structure (Herrmann et al., 2021; Komor et al., 1988). Unfortunately, the lack of radiometric dating and the significant erosion in the central uplift, which has led to the removal of the shallowest hydrothermal products (e.g., Hode et al., 2003; Holm-Alwmark et al., 2017), complicate the interpretation of samples from the Siljan area. In addition, the Siljan impact structure is located between the Transscandinavian Igneous Belt complex and the westernmost domain of the Svecofennian crust (e.g., Herrmann et al., 2021). This area has experienced complex geological histories, including compression, shearing, and extension of crustal blocks (e.g., Sandström and Tullborg, 2009; Tillberg et al., 2021). Major events of fracturing and/or reactivation of fractures associated with mineralization have been identified (e.g., Sandström and Tullborg, 2009; Tillberg et al., 2021), such as fluid circulation related to local magmatism corresponding to the formation of the Dala granites during the late stage of the Svecokarelian orogeny (1.9–1.7 Ga, Herrmann et al., 2021). Other possible fluid circulations include those during the early phase of the Hallandian-Danopolonian extensional event (1.5–1.4 Ga, Brander and Söderlund, 2009; Lundmark and Lamminen, 2016), the Sveconorwegian orogeny (active between 1140 and 980 Ma, Bingen et al., 2005), and the far-field effects of the Caledonian orogeny (main stage of collision and orogenic collapse between 430 and 380 Ma, Corfu et al., 2014).

2.2. Samples description

In this study, we analyzed exposed bedrock samples from the Siljan impact structure collected and previously studied by Holm et al. (2011) and Holm-Alwmark et al. (2017). We focused on the sampled lithologies that represent igneous rocks (granitic and volcanic rocks) representing the Svecokarelian and post-Svecokarelian provinces (Fig. 1). The samples are fine to coarse-grained, of red colour (see macroscopic pictures in **supplementary data**). The mineral assemblage is dominated by potassium feldspar (K-feldspar), plagioclase feldspar, quartz, hornblende, and biotite (see thin section photomicrographs in Fig.2). Five samples across the Siljan crater were analyzed to highlight the evolution between the center and the rim of the structure (Fig.1 and Table 1). Selected samples show a shock pressure ranging from 0 to 20 GPa (Holm et al., 2011).

Samples from the two types of igneous rocks present at Siljan were analyzed: SIL19, SIL59, and SIL61 for the Svecokarelian province, and SIL34 and SIL20 for the post-Svecokarelian province. SIL19 is a porphyry (porphyritic volcanic rock) composed of K-feldspars and quartz grains around 1 mm in a fine-grained matrix. It is the most distal sample from the center of the impact structure (16 km from center) investigated here and it shows no evidence of shock (Holm et al., 2011). Two bulk fractions of this sample were analyzed (SIL19 and SIL19-B). SIL34 is a porphyritic granite composed of biotite, K-feldspar, hornblende, and quartz grains of 2–5 mm. It is located close to the impact crater's North rim (10 km from center) and recorded a shock pressure of 2–5 GPa (Holm et al., 2011). We measured a bulk fraction and a pure quartz fraction (SIL34 and SIL34-Q) separated from this sample. SIL20 is a fine-grained granitic sample composed of quartz, K-feldspar, biotite, and hornblende. It is located close to the southern part of the central plateau (11 km from center), with a recorded shock pressure of 5–10 GPa and containing approximately 10 % of quartz grains with

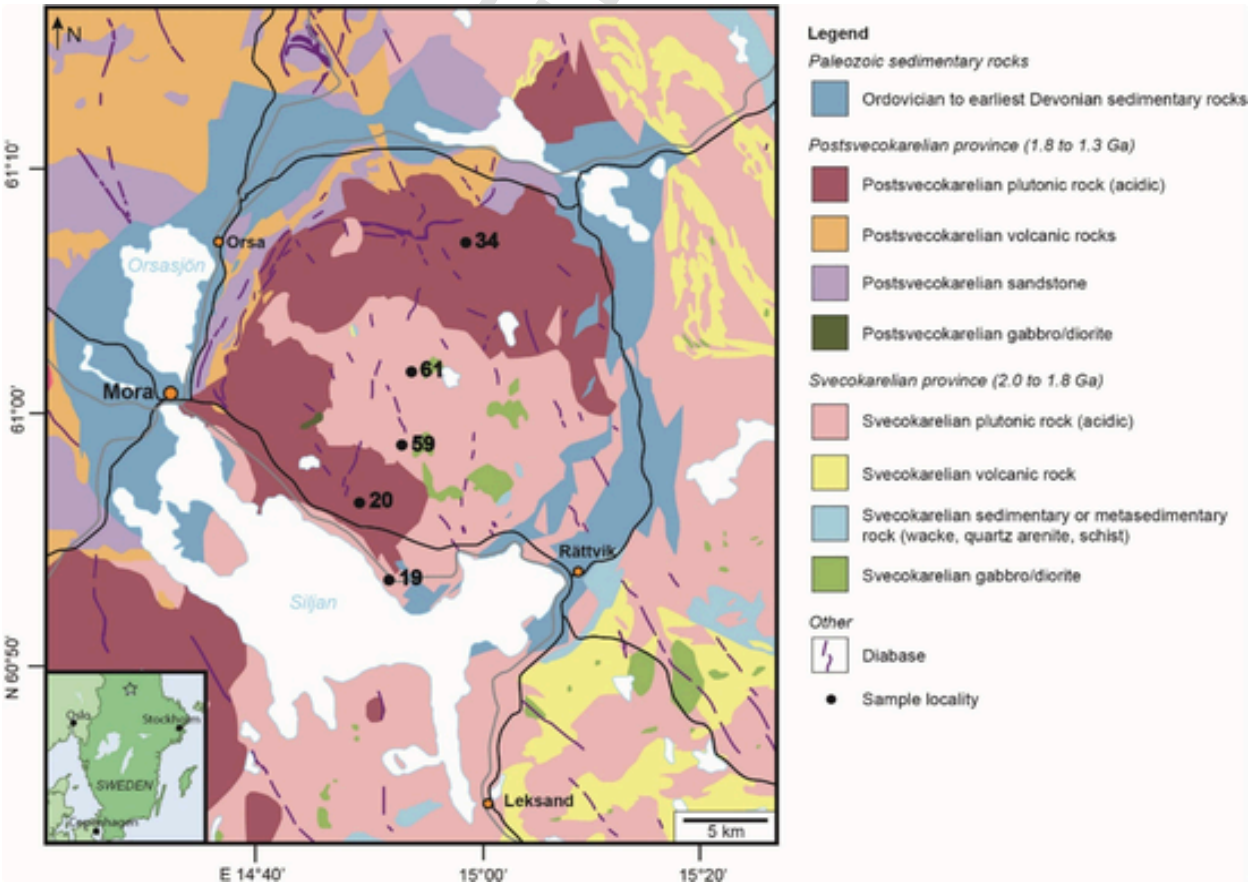

Fig. 1. Location of studied samples on a simplified geologic map of the Siljan impact structure. The map is modified after the Swedish Geological Survey (SGU) bedrock map viewer [https://apps.sgu.se/kartvisare/kartvisare-berg-50-250-tusen.html]; Holm et al. (2011); Holm-Alwmark (2021); Holm-Alwmark et al. (2022). Ages of units are from the SGU bedrock map viewer and Stephens (2020).

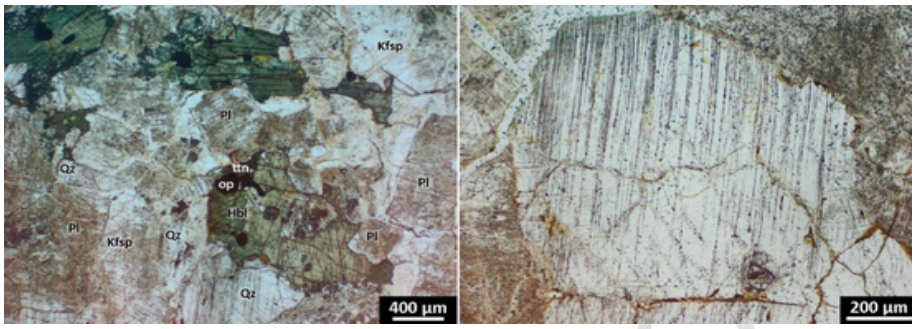

Fig. 2. Thin section photomicrographs (crossed polars) of shocked bedrock from the Siljan structure (example of SIL61). a) Photomicrograph showing the mineralogy and texture of sample SIL61. b) Quartz grain from sample SIL61 with decorated PDF sets. Kfsp = K-feldspar; Hbl = hornblende; Qz = quartz; Pl = plagioclase; ttn = titanite; op = opaque.

Table 1
Names, locations from the center of the impact structure, recorded shock pressures, types of Dala granites, rock types, lists of the major minerals, grain sizes, % of shocked quartz, and the targets of the analyses done on samples selected for this study (based on Holm et al., 2011).

Sample name	Distance from the center	Estimated Pressure	Types of Dala granite	Rock type	Major minerals list	Grain size	% of shocked quartz	Target of the analysis
SIL19	16 km	–	Svecokarelian	Fine-grained porphyry	K-feldspar (Quartz)	< 1 mm	0 %	Whole rock
SIL34	10 km	2–5 GPa	post-Svecokarelian	Porphyritic granite	K-feldspar / Quartz Biotite / Amphibole	2–10 mm	0 %	Whole rock **Quartz fraction**
SIL20	11 km	5–10 GPa	post-Svecokarelian	Fine-grained granite	K-feldspar / Quartz Biotite / Amphibole	< 1 mm	10 %	Whole rock
SIL59	7 km	10–15 GPa	Svecokarelian	Porphyritic granite	K-feldspar / Quartz Biotite / Amphibole	2–10 mm	100 %	Whole rock **Quartz fraction**
SIL61	2 km	15–20 GPa	Svecokarelian	Porphyritic granitoid	K-feldspar / Biotite Amphibole (Quartz)	2–10 mm	100 %	Whole rock

PDFs (Holm et al., 2011). We analyzed two bulk fractions of this sample (SIL20 and SIL20-B). SIL59 is a porphyritic granite composed of biotite, K-feldspar, hornblende, and quartz grains of 2–5 mm. It is located approximately at 7 km from the center of the impact structure and recorded a shock pressure of 10–15 GPa, with 100 % of the quartz grains being shocked (Holm et al., 2011). We conducted analyses on both a bulk fraction and a pure quartz fraction (SIL59 and SIL59-Q) from this sample. Lastly, SIL61 is a porphyritic granitoid composed of biotite and K-feldspars grains of 2–5 mm, with few observable quartz grains. It is the closest sample to the center of the impact structure (2 km from center) and it was subjected to shock pressures of 15–20 GPa, with 100 % of the observed quartz grains displaying shock-induced features (Holm et al., 2011). We analyzed one fraction from this sample.

2.3. Method description

Whole rock samples (SIL19, SIL34, SIL20, SIL59, and SIL61), and separated quartz crystals from two samples (SIL34 and SIL59) were analyzed. Noble gases elemental abundances and isotopic compositions (Ne, Ar, Xe, and Kr) in fluid inclusions contained in these samples were determined by stepwise crushing under high vacuum (Table 2 and **Supp. Table 1**).

Before noble gas analyses, selected sample fragments were crushed in a metal mortar to obtain granulometric fractions ranging from 1 to 3 mm in size. Indeed, this is the ideal range of size to minimize the adsorption of air on the surface of the grains. Also, larger grains were avoided to prevent the presence of hidden impurities or of atmospheric gases trapped in fractures between minerals. Smaller grains were rejected because of the possibility of opening some of the largest fluid inclusions prior to analysis. For two samples showing high-purity crystal grains of significant size, quartz crystals were manually hand-picked under a binocular microscope to ensure the absence of impurities at the surface or inside individual crystals. Finally, grains were subsequently cleaned with acetone in an ultrasonic bath, then rinsed with acetone, and dried under a heating lamp for 30 min. Between 250 mg and 2 g of sample were then loaded inside each crusher for noble gas analyses/measurements. Once loaded into the ultra-high vacuum crusher, the samples were baked at 120 °C overnight, to remove any contribution from atmospheric gases adsorbed on the grains' surfaces. Higher temperatures were avoided to prevent rupture of fluid inclusions by thermal decrepitation.

The stainless-steel crusher consists of a stainless tube containing an iron ball which allows crushing the sample by manually lifting the iron ball up and projecting it down with an external magnet. In this study, we applied between 3 and 5 crushing steps with an increasing number of strokes by step (going from 10 to 300 strokes) on each sample to extract all the gases contained in the studied fractions. Noble gases released from fluid inclusions for each crushing step were purified using three getters, including a St707 (SAES) Non-Evaporable Getter (Zr-V-Fe) at 450 °C and two Ti-sponge getter pumps at 650 °C, during 5 min at high temperature and then cooled down to room temperature over 10 min to remove the major reactive volatile species (e.g., H_2O, CO_2, N_2, etc.). The purified noble gases were then cryogenically trapped at 20 K on a cryogenic trap and sequentially released at 77 K for Ne, 165 K for Ar, 198 K for Kr, and 335 K for Xe. Ar, Kr, and Xe gas fractions released at given temperatures from the charcoal in contact with the cryogenic stage were trapped on a charcoal cooled down to liquid nitrogen temperature in order to maximize gas recovery and efficiency of gas separation (e.g., Broadley and Bekaert, 2024). Finally, each gas fraction was introduced into a static noble gas mass spectrometer (Noblesse, Ametek/NuInstruments) to be analyzed. During the purification sequence, the Ar fraction was stored in a dedicated volume and was measured only at the end of the measurement sequence in an attempt to avoid any interference of significant quantities of radiogenic ^{40}Ar with the measurement of krypton isotopes.

Table 2

Names, locations from the center of the impact structure, recorded shock pressures, % of shocked quartz with planar deformation features (PDF), abundances (in units of cm^3 STP g^{-1}), isotopic ratios of Ne, Ar, Kr, and Xe, elemental ratios, and F values for ^{20}Ne, ^{84}Kr, and ^{130}Xe from the total gas released during crushing experiments on Siljan samples analyzed during this study. Isotopic ratios for the atmosphere are from (Lee et al., 2006; Ozima and Podosek, 2002). Errors at 1σ.

Sample	Distance to center	Shock Pressure	PDF		^{22}Ne ($x10^{-11}$)	±	$^{20}Ne/^{22}Ne$	±	$^{21}Ne/^{22}Ne$	±		^{36}Ar ($x10^{-10}$)	±	$^{40}Ar^*$ ($x10^{-6}$)	±	$^{38}Ar/^{36}Ar$	±	$^{40}Ar/^{36}Ar$	±
SIL19	16 km	No shock	0 %	Neon	5.56	0.38	9.61	0.03	0.0334	0.0005	Argon	7.94	0.85	5.19	0.54	0.1880	0.0016	6830	150
SIL19-B					2.75	0.15	9.83	0.04	0.0319	0.0004		4.75	0.26	3.40	0.18	0.1883	0.0011	7470	130
SIL34	10 km	2–5 GPa	0 %		38.69	2.03	9.68	0.03	0.0299	0.0003		99.26	1.42	4.71	0.07	0.1896	0.0008	775	5
SIL34-Q					4.16	0.37	9.73	0.10	0.0349	0.0007		8.46	0.86	3.58	0.37	0.1879	0.0018	4530	60
SIL20	11 km	5–10 GPa	10 %		13.02	0.51	9.71	0.03	0.0294	0.0003		32.63	0.62	42.85	0.83	0.1872	0.0007	13,450	80
SIL20-B					15.47	0.66	9.71	0.03	0.0306	0.0003		27.71	0.84	68.47	2.10	0.1875	0.0008	25,000	110
SIL59	7 km	10–15 GPa	100 %		45.21	1.75	9.68	0.03	0.0303	0.0003		66.90	1.27	10.53	0.25	0.1888	0.0007	1870	20
SIL59-Q					57.96	0.97	9.47	0.04	0.0354	0.0003		70.37	2.37	18.01	0.79	0.1871	0.0012	2860	60
SIL61	2 km	15–20 GPa	100 %		2.34	0.15	9.74	0.03	0.0293	0.0005		3.86	0.37	0.70	0.07	0.1887	0.0015	2110	45
Air							**9.80**	**0.08**	**0.0290**	**0.0003**						**0.1885**	**0.0003**	**298.56**	**0.31**

Sample		^{84}Kr ($x10^{-11}$)	±	$^{78}Kr/^{84}Kr$ ($x10^{-3}$)	±	$^{80}Kr/^{84}Kr$ ($x10^{-2}$)	±	$^{82}Kr/^{84}Kr$ ($x10^{-1}$)	±	$^{83}Kr/^{84}Kr$ ($x10^{-1}$)	±	$^{86}Kr/^{84}Kr$ ($x10^{-1}$)	±
SIL19	Krypton	1.33	0.16	5.962	0.122	4.215	0.029	2.0300	0.0107	2.008	0.009	3.069	0.015
SIL19-B		0.99	0.05	6.160	0.071	5.275	0.072	2.0220	0.0053	2.015	0.005	3.061	0.008
SIL34		30.45	0.90	5.999	0.050	4.285	0.022	2.0102	0.0037	2.006	0.004	3.063	0.005
SIL34-Q		4.67	0.21	6.146	0.063	4.609	0.035	2.0052	0.0049	1.995	0.005	3.071	0.007
SIL20		13.70	0.32	6.081	0.042	7.575	0.133	1.9980	0.0030	1.999	0.003	3.082	0.005
SIL20-B		10.29	0.28	6.207	0.050	11.056	0.312	1.9971	0.0035	1.997	0.004	3.088	0.005
SIL59		18.08	0.42	5.906	0.041	3.983	0.012	2.0157	0.0031	2.009	0.003	3.056	0.005
SIL59-Q		15.85	0.49	6.024	0.052	4.027	0.015	2.0169	0.0039	2.015	0.004	3.051	0.006
SIL61		2.50	0.08	6.082	0.054	4.028	0.015	2.0157	0.0041	2.009	0.004	3.072	0.006
Air				**6.087**	**0.020**	**3.960**	**0.002**	**2.0217**	**0.0004**	**2.014**	**0.002**	**3.052**	**0.003**

Sample		^{130}Xe ($x10^{-13}$)	±	$^{124}Xe/^{130}Xe$	±	$^{126}Xe/^{130}Xe$	±	$^{128}Xe/^{130}Xe$	±	$^{129}Xe/^{130}Xe$	±	$^{131}Xe/^{130}Xe$	±	$^{132}Xe/^{130}Xe$	±	$^{134}Xe/^{130}Xe$	±	$^{136}Xe/^{130}Xe$	±
SIL19	Xenon	1.26	0.18	0.0236	0.0021	0.0198	0.0017	0.4665	0.0106	6.562	0.088	5.290	0.072	6.920	0.093	2.888	0.046	2.560	0.050
SIL19-B		0.94	0.06	0.0241	0.0011	0.0223	0.0012	0.4724	0.0060	6.554	0.061	5.261	0.042	6.829	0.057	2.807	0.030	2.518	0.028
SIL34		23.64	0.80	0.0222	0.0008	0.0217	0.0008	0.4728	0.0038	6.530	0.035	5.231	0.025	6.651	0.031	2.588	0.014	2.211	0.015
SIL34-Q		2.59	0.22	0.0227	0.0013	0.0199	0.0013	0.4696	0.0073	6.435	0.061	5.179	0.049	6.657	0.064	2.669	0.027	2.323	0.029
SIL20		6.72	0.19	0.0222	0.0007	0.0210	0.0007	0.4710	0.0039	6.489	0.036	5.271	0.028	7.037	0.037	3.201	0.025	2.955	0.027
SIL20-B		6.02	0.19	0.0219	0.0008	0.0211	0.0008	0.4709	0.0045	6.529	0.041	5.323	0.030	7.228	0.046	3.418	0.033	3.204	0.038
SIL59		14.18	0.39	0.0220	0.0008	0.0202	0.0007	0.4715	0.0041	6.497	0.038	5.201	0.028	6.613	0.035	2.591	0.017	2.232	0.016
SIL59-Q		10.02	0.53	0.0234	0.0010	0.0215	0.0010	0.4725	0.0054	6.547	0.048	5.229	0.036	6.713	0.050	2.675	0.024	2.318	0.023
SIL61		4.50	0.13	0.0232	0.0009	0.0212	0.0009	0.4667	0.0041	6.500	0.038	5.219	0.029	6.664	0.036	2.576	0.017	2.217	0.017
Air				**0.0234**	**0.0001**	**0.0218**	**0.0001**	**0.4715**	**0.0007**	**6.496**	**0.009**	**5.213**	**0.008**	**6.607**	**0.005**	**2.563**	**0.004**	**2.176**	**0.003**

Sample		$^{20}Ne/^{36}Ar$	±	$^{84}Kr/^{36}Ar$ ($x10^{-2}$)	±	$^{130}Xe/^{36}Ar$ ($x10^{-4}$)	±		$F(^{20}Ne/^{36}Ar)_{air}$	±	$F(^{84}Kr/^{36}Ar)_{air}$	±	$F(^{130}Xe/^{36}Ar)_{air}$	±
SIL19	Elemental ratios	0.673	0.085	1.68	0.27	1.59	0.28	F value	1.28	0.16	0.81	0.13	1.41	0.25
SIL19-B		0.571	0.043	2.09	0.15	1.98	0.16		1.09	0.08	1.01	0.07	1.75	0.14
SIL34		0.377	0.021	3.07	0.10	2.38	0.09		0.72	0.04	1.48	0.05	2.11	0.08
SIL34-Q		0.478	0.065	5.52	0.61	3.06	0.40		0.91	0.12	2.67	0.30	2.71	0.36
SIL20		0.387	0.017	4.20	0.13	2.06	0.07		0.74	0.03	2.03	0.06	1.82	0.06
SIL20-B		0.542	0.028	3.71	0.15	2.17	0.10		1.03	0.05	1.79	0.07	1.92	0.08
SIL59		0.654	0.028	2.70	0.08	2.12	0.07		1.25	0.05	1.31	0.04	1.88	0.06
SIL59-Q		0.781	0.030	2.25	0.10	1.42	0.09		1.49	0.06	1.09	0.05	1.26	0.08
SIL61		0.591	0.069	6.47	0.66	11.66	1.18		1.13	0.13	3.12	0.32	10.32	1.04
Air		**0.524**	**0.001**	**2.07**	**0.02**	**1.13**	**0.01**		**1.00**		**1.00**		**1.00**	

Neon was the first gas to be analyzed in multi-collection mode using electron multipliers as detectors. CO_2^+ (m = 44) and $^{40}Ar^+$ (m = 40) signals were also measured after each Ne integration cycle in order to correct ^{22}Ne (m = 21.991) and ^{20}Ne (m = 19.992) signals for the contributions from CO_2^{++} (m = 21.995) and $^{40}Ar^{++}$ (m = 19.981) signals using double ionization ratios (Zimmermann et al., 2015).

Then, Kr isotopes were measured in peak jumping mode using one electron multiplier. Xe was subsequently analyzed using a similar procedure. Finally, Ar was analyzed in multi-collection mode using a faraday cup for the detection of ^{40}Ar and electron multipliers for ^{36}Ar and ^{38}Ar.

Measurements of standard aliquots taken from a standard bottle filled with diluted air were conducted before and after each sample analysis. The standard measurement followed the same analytical procedure as the samples and provided an accurate definition of mass discrimination and sensitivity of the noble gas mass spectrometer, and reproducibility of the entire analytical procedure.

Furthermore, procedural blank analyses were monitored before each sample analysis and were determined by letting the gas accumulate in the crusher and the purification line without crushing the sample. Blank analyses done previously with about 100 strokes applied to an empty crusher similar the one use in this study did not lead to a significant increase of the amount of blank. The blank average during our experiments reaches 1.2×10^{-12} cm^3 STP for ^{22}Ne, 3.2×10^{-11} cm^3 STP for ^{36}Ar, 5.8×10^{-13} cm^3 STP for ^{84}Kr, and 7.5×10^{-15} cm^3 STP for ^{130}Xe.

A full propagation of the errors on the internal precision, the sensitivity of the mass spectrometer, the reproducibility of the standards (see **Supp. Table 2**), and the blank contribution has been applied in order to take into account all potential sources of variability (e.g., Bekaert et al., 2017).

3. Results

Abundances and isotopic compositions of the total noble gases (Ne, Ar, Kr, and Xe) released by crushing step of Siljan samples are given in Table 2, as well as the elemental ratios and F values, which represent the relative noble gas abundances normalized to ^{36}Ar and the ratio normalized to that of air (Burnard et al., 2013):

$$F(i) = \frac{\left(i/^{36}Ar\right)_{sample}}{\left(i/^{36}Ar\right)_{air}}$$

Results obtained for each crushing step are reported in the **Supplementary Tables**.

3.1. Isotope abundances in Siljan samples

Fig. 3 shows the total amounts of noble gases released during the crushing experiments of each Siljan sample, in the range 2-56 $\times 10^{-11}$ cm^3 STP g^{-1} of ^{22}Ne, 4-99 $\times 10^{-10}$ cm^3 STP g^{-1} of ^{36}Ar, 1-30 $\times 10^{-11}$ cm^3 STP g^{-1} of ^{84}Kr, and 1-24 $\times 10^{-13}$ cm^3 STP g^{-1} of ^{130}Xe (Table 2). Noble gas abundances for individual crushing steps range from 0.4 to 20.1 $\times 10^{-11}$ cm^3 STP g^{-1} for ^{22}Ne (4 to 116 times the blank level), 0.6–44.8 $\times 10^{-10}$ cm^3 STP g^{-1} for ^{36}Ar (3 to 99 times the blank level), 0.2–13.1 $\times 10^{-11}$ cm^3 STP g^{-1} for ^{84}Kr (3 to 161 times the blank level), and 0.1–9.5 $\times 10^{-13}$ cm^3 STP g^{-1} for ^{130}Xe (2 to 92 times the blank level) (see **Supp. Tables**). Procedural blanks in this study were higher than usual (Avice et al., 2023). This could be due to desorption of gases adsorbed or trapped in fractures of the Siljan samples. This is particularly true for SIL19, SIL19-B, SIL34-Q, and SIL61 (see **Supp. Tables**). Crushing steps for SIL19, SIL19-B, SIL34-Q, and SIL61 samples released from 0.4 to 2.1 $\times 10^{-11}$ cm^3 STP g^{-1} of ^{22}Ne (4 to 19 times the blank level), 0.6–3.9 $\times 10^{-10}$ cm^3 STP g^{-1} of ^{36}Ar (3 to 14 times the blank level),

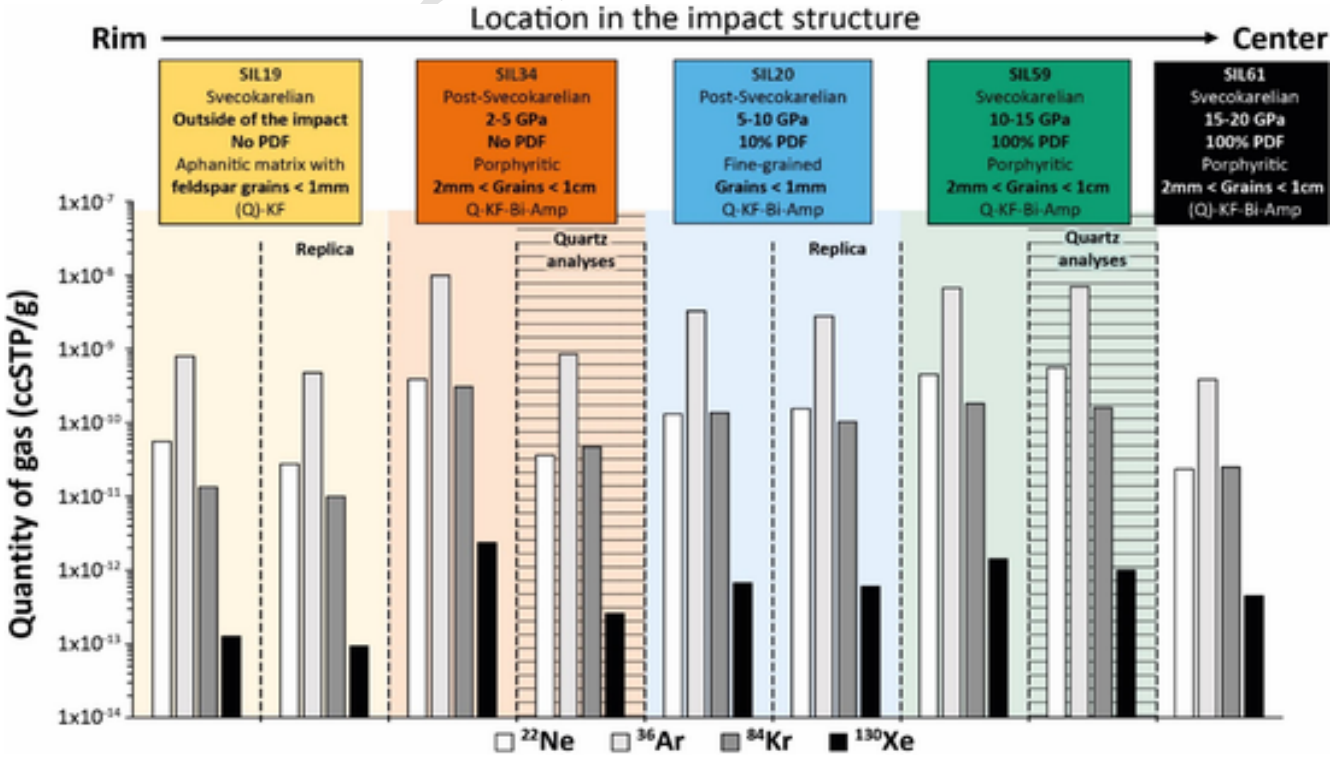

Fig. 3. Histogram plots representing the total amounts of noble gases (Ne, Ar, Kr, and Xe) released during the crushing experiments of Siljan samples (Table 2). The samples are classified according to their distance to the center of the impact structure, and their shock pressure range defined by Holm et al. (2011).

0.2–1.9 × 10^{-11} cm^3 STP g^{-1} of ^{84}Kr (3 to 21 times the blank level), and 0.2–1.5 × 10^{-13} cm^3 STP g^{-1} of ^{130}Xe (2 to 29 times the blank level).

There is no clear relationship between the gas amounts measured and the relative distance from the center of the impact structure where the samples were collected (Fig.3), neither with the relative shock pressure recorded by the samples, or with the amount of shocked quartz grains in the samples (Holm et al., 2011). However, there is a significant increase of the amounts of gases released with increasing grain size, except for sample SIL61 (with a low amount of quartz grains) and for the quartz fraction of SIL34 (without PDFs).

3.2. Elemental abundances

Fig. 4 shows F(^{20}Ne), F(^{84}Kr), and F(^{130}Xe) values for all Siljan samples, which represent measured $^{20}Ne/^{36}Ar$, $^{84}Kr/^{36}Ar$, and $^{130}Xe/^{36}Ar$ ratios normalized to corresponding air values (dashed red line, Fig.4). Meteoric water (0 °C) and seawater are characterized by atmospheric noble gas isotopic ratios. They have different abundance ratios ($^{20}Ne/^{36}Ar$, $^{84}Kr/^{36}Ar$, $^{130}Xe/^{36}Ar$), because noble gas solubility is influenced by temperature and salinity (Smith and Kennedy, 1983). Meteoric water and seawater are characterized by enrichment in heavy/light noble gases relative to air (Smith and Kennedy, 1983), and it is difficult to distinguish meteoric water from seawater based solely on noble gas abundance ratios. These fluids are thus commonly referred to as Air Saturated Water (ASW) (Kendrick and Burnard, 2013). Based on previous studies (Komor et al., 1988; Lindblom and Wickman, 1985), meteoric water or non to low-saline water is probably the major component here (represented as a dashed blue line in Fig. 4).

For most samples, F(^{20}Ne), F(^{84}Kr), and F(^{130}Xe) values for all the gas released during the experiment of Siljan samples lie between meteoric water and air values (Fig.4). We observed an enrichment in F(^{20}Ne) and a depletion in F(^{84}Kr) and F(^{130}Xe) values compared to the initial meteoric water values. Nevertheless, compared to the meteoric water values, sample SIL61 presents higher F(^{84}Kr) and F(^{130}Xe) values, SIL34-Q presents higher F(^{84}Kr) value, and SIL19 and SIL19-B present lower F(^{84}Kr) values. Note that the F(^{20}Ne) value is close to the atmospheric end-member.

3.3. Neon and argon

$^{20}Ne/^{22}Ne$ ratios range from 9.3 to 9.9, and from 0.027 to 0.038 for $^{21}Ne/^{22}Ne$ ratio (atmospheric ratios: $^{20}Ne/^{22}Ne$ = 9.8, $^{21}Ne/^{22}Ne$ = 0.029; Eberhardt et al., 1965) (**Supp. Table 1**). Neon isotopic ratios are presented in a three-isotopes diagram (Fig.5) and are compared to a typical air-MORB mantle neon mixing line (MORB data: $^{20}Ne/^{22}Ne \sim 12.5$, $^{21}Ne/^{22}Ne \sim 0.06$; Moreira et al., 1998), to the modern crustal Ne mixing line (Kennedy et al., 1990), and to the Archean crustal mixing lines (Lippmann-Pipke et al., 2011). Furthermore, Fig. 5 shows nucleogenic Ne lines starting at air composition, with $^{21}Ne/^{22}Ne$ ratios of 0.2 and 0.1 (intersection point for x-axis at ^{20}Ne = 0). These mixing lines of air and nucleogenic Ne are plotted in order to compare our data with possible nucleogenic ^{22}Ne contribution. Neon isotopic ratios for each crushing step are close to but lower than the present-day atmosphere composition and seem to fall between the Modern crustal Ne mixing line and the nucleogenic line, with a corresponding nucleogenic $^{21}Ne/^{22}Ne$ ratio of 0.1.

Argon isotope data are shown in Fig. 6. $^{40}Ar/^{36}Ar$ ratios are higher than the atmospheric value (298.56; Lee et al., 2006) and range from 562 ± 3 (crushing step #1 for sample SIL34) to 27,250 ± 200 (crushing step #2 for sample SIL20-B) (**Supp. Table 1**). By contrast, $^{38}Ar/^{36}Ar$ ratios do not show any significant deviation from the isotopic composition of the modern atmosphere (0.1885; Lee et al., 2006).

Fig. 7 shows a plot of $^{40}Ar/^{36}Ar$ ratios versus $1/^{36}Ar$ values for the total gas released during the experiment of each Siljan sample. Gas-poor samples (with elevated $1/^{36}Ar$ ratios) have high $^{40}Ar/^{36}Ar$ ratios and are dominated by the contribution of a radiogenic end-member. Gas-rich samples (low $1/^{36}Ar$ ratios) show an isotopic composition of argon closer to the air values. Lower $^{40}Ar/^{36}Ar$ and $1/^{36}Ar$ values point

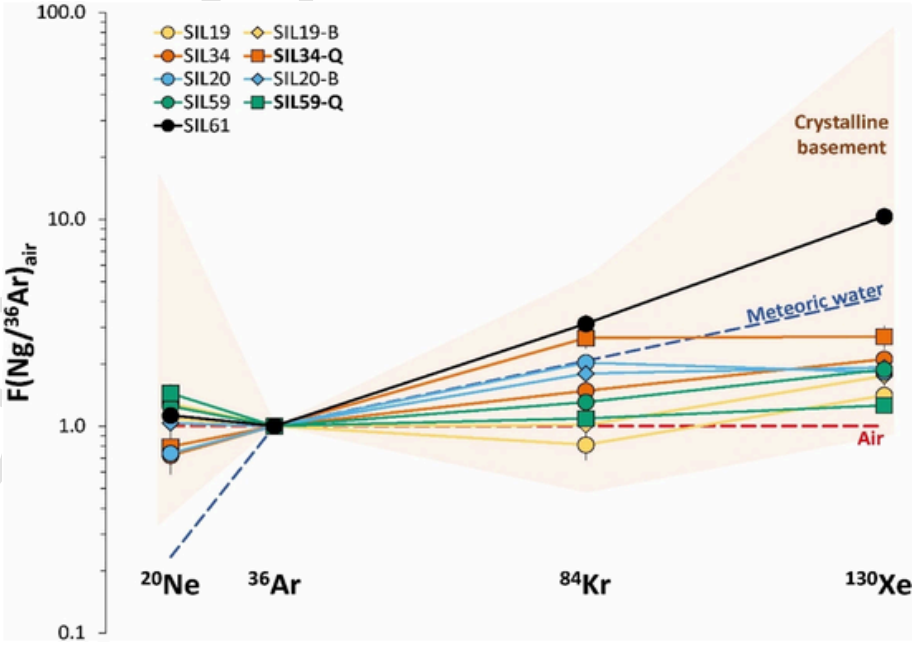

Fig. 4. Noble gas relative abundance patterns for the total gas released from Siljan samples (Table 2). Abundance ratios are normalized to air: $F(Ng/^{36}Ar)_{air} = (Ng/^{36}Ar)_{sample}/(Ng/^{36}Ar)_{air}$; such that Air = 1; Ng = ^{20}Ne, ^{84}Kr or ^{130}Xe. The dashed blue line represents the meteoric water composition (0 °C), and the orange area shows the range of elemental ratios of noble gases in rocks from the crystalline basement (Kendrick and Burnard, 2013; Ozima and Podosek, 2002). (For interpretation of the references to colour in this figure legend, the reader is referred to the web version of this article.)

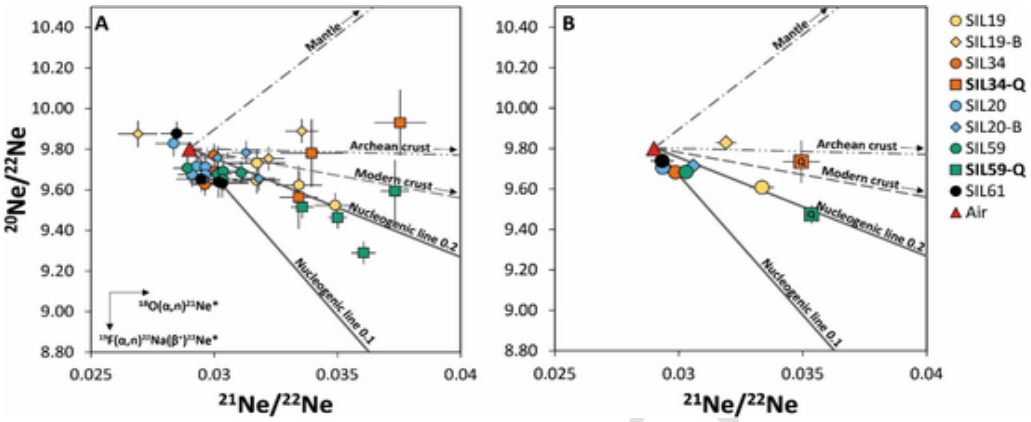

Fig. 5. Three-isotope plot of Ne for crushing experiments on Siljan samples (see data in Table 2 and Supp. Table 1). These graphics show the results for (A) each crushing step, and (B) the total gas released during the experiment of each sample. Diamonds represent the duplicated analyses for SIL19 and SIL20 samples, and squares represent analyses obtained on quartz separated from samples SIL34 and SIL59. The red triangle represents the isotopic composition of atmospheric neon. The dot-dashed line represents the Ne mixing between atmospheric and MORB mantle components (MORB data: $^{20}Ne/^{22}Ne \sim 12.5$, $^{21}Ne/^{22}Ne \sim 0.06$; Moreira et al., 1998). The dashed line represents the Modern crustal Ne mixing line corresponding to the addition of crustal nucleogenic Ne (Kennedy et al., 1990). The Archean mixing line (double dot-dashed line) is from analyses by Lippmann-Pipke et al. (2011). Nucleogenic Ne lines intercepting the x-axis at $^{21}Ne/^{22}Ne$ ratios of 0.1 and 0.2 are represented by continuous lines. All nucleogenic Ne lines start at air composition. Errors are at 1σ. (For interpretation of the references to colour in this figure legend, the reader is referred to the web version of this article.)

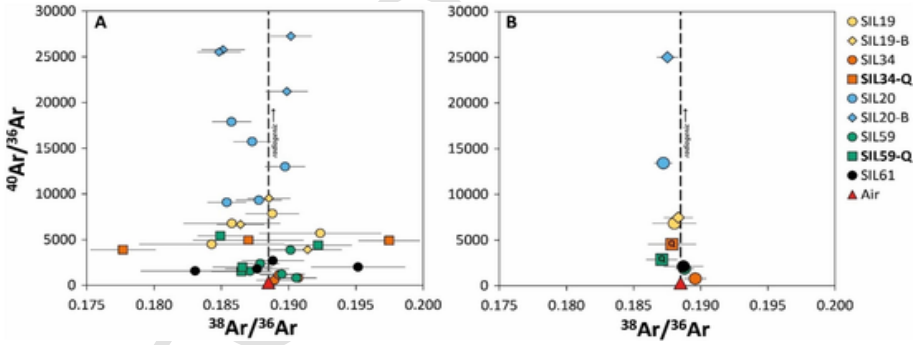

Fig. 6. Three-isotope plot of Ar for crushing experiments on Siljan samples (see data in Table 2 and Supp. Table 1). These graphics show the results for (A) each crushing step, and (B) the total gas released during the experiment for each sample. Diamonds represent the duplicated analysis on SIL19 and SIL20 samples, and squares represent the analyses obtained on quartz separated from samples SIL34 and SIL59. The red triangle represents the $^{40}Ar/^{36}Ar$ and $^{38}Ar/^{36}Ar$ ratios of the atmosphere (Lee et al., 2006). The dashed line represents the atmospheric $^{38}Ar/^{36}Ar$ ratio of 0.1885. Errors are at 1σ. (For interpretation of the references to colour in this figure legend, the reader is referred to the web version of this article.)

to a greater atmospheric contribution, while higher values reflect the addition of crustally produced radiogenic ^{40}Ar ($^{40}Ar^*$) with less atmospheric contribution (Kennedy et al., 1985).

Furthermore, the $^{40}Ar/^{36}Ar$ ratio, and thus the $^{40}Ar^*$, for fine-grained samples (SIL19 and SIL20) are significantly higher than those of the coarse-grained samples (SIL34, SIL59, and SIL61) (Figs.6 and 7).

3.4. Krypton and xenon

The isotopic compositions of Kr in Siljan samples are reported in Table 2 and are displayed in Fig. 8 where the isotopic ratios are normalized to ^{84}Kr and expressed with the delta notation relative to the isotopic composition of the modern atmosphere (**Supp. Table 1**). $^{80}Kr/^{84}Kr$ ratios show an important contribution from interfering ^{40}Ar (Meshik et al., 2014) present in the Siljan samples, and are thus not shown in Fig. 8 nor discussed further. A slight enrichment on ^{86}Kr compared to atmospheric data can be observed, a depletion on light isotopes can also be observed (^{82}Kr, ^{83}Kr), and an important dispersion can be noted on ^{78}Kr.

Results for Xe isotopic ratios and abundances obtained from the total gas released during the experiments for each sample of Siljan are presented in Table 2. Fig. 9 shows the isotopic ratios normalized to ^{130}Xe and expressed with the delta notation relative to the isotopic composition of the modern atmosphere obtained from Siljan samples (see **Supp. Table 1**). We can observe an enrichment in heavy isotopes ($^{131\text{-}136}Xe$) relative to the isotopic composition of the modern atmosphere, especially for fine-grained samples SIL19 and SIL20. Other isotopic ratios ($^{128\text{-}129}Xe/^{130}Xe$) are, within errors, identical to the composition of xenon in the modern atmosphere. $^{124\text{-}126}Xe/^{130}Xe$ show a larger dispersion.

4. Discussion

4.1. Detection of an atmospheric component in Siljan samples

Fig. 10 shows the F values of ^{84}Kr and ^{130}Xe, representing measured $^{84}Kr/^{36}Ar$ and $^{130}Xe/^{36}Ar$ ratios, normalized to corresponding air values. Most values are distributed between air and meteoric water

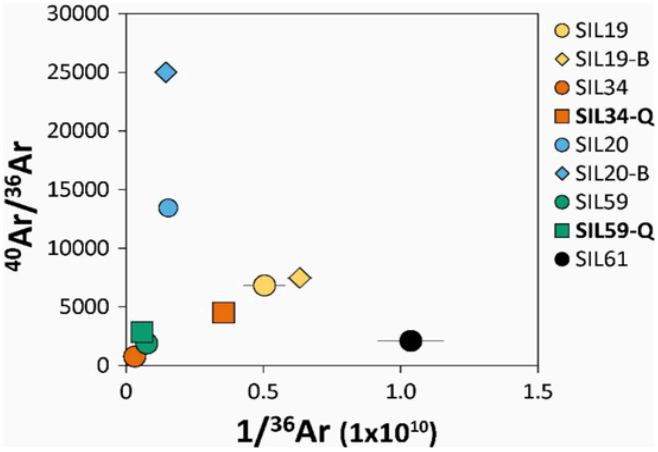

Fig. 7. $^{40}Ar/^{36}Ar$ versus $1/^{36}Ar$ for the total gas released during the experiment of each Siljan sample. Diamonds represent duplicated analysis on SIL19 and SIL20 samples, and squares represent the analyses obtained on quartz separated from samples SIL34 and SIL59.

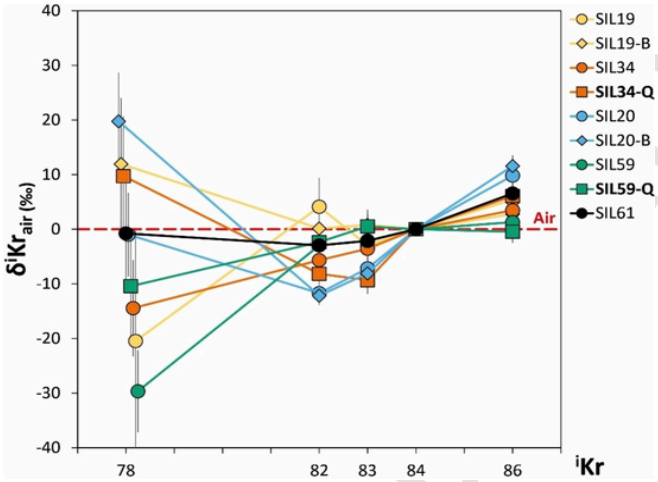

Fig. 8. Isotopic spectra of Kr from the total gas released during the experiment of each sample of Siljan (see data in Table 2 and Supp. Table 1). Isotopic compositions are displayed using the delta notation normalized to ^{84}Kr and to the isotopic composition of the modern atmosphere (Ozima and Podosek, 2002). $\delta^{i}Kr_{air} = 1000 \times \left(\frac{(^{i}Kr/^{84}Kr)\ sample}{(^{i}Kr/^{84}Kr)\ air} - 1 \right)$. Errors are at 1σ. The mass ^{80}Kr is affected by the presence of interfering ^{40}Ar, and it is not represented in this graph. Delta values for ^{78}Kr are slightly shifted for better visibility.

noble gas elemental abundances values, suggesting that some atmospheric signal has been incorporated. This is confirmed by the fact that neon, argon, krypton, and xenon isotopic ratios are relatively close to the atmospheric composition.

Furthermore, the $^{20}Ne/^{22}Ne$ ratio is close to the atmosphere, but stay lower, and the $^{38}Ar/^{36}Ar$ ratios show no deviation from the atmospheric value (0.1885; Lee et al., 2006). This demonstrates that light noble gases (Ne, Ar) did not suffer from isotopic fractionation.

4.2. Origin of non-atmospheric fluids

Siljan samples show a clear contribution from crustal fluids, which were either originally present in the samples before the impact or were

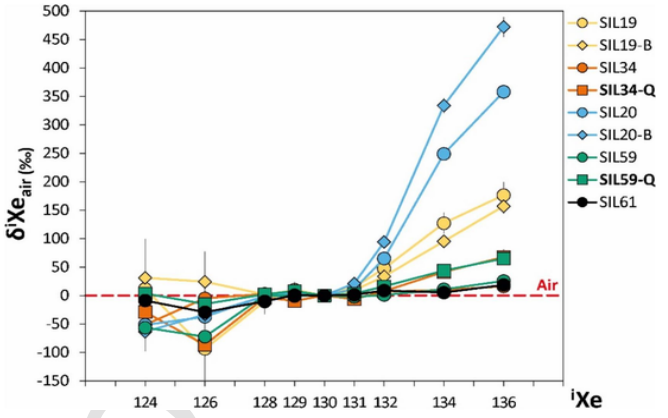

Fig. 9. Isotopic spectra of Xe from the total gas released during the experiment of each sample of Siljan (Supp. Table 1). Isotopic compositions are given using the delta notation normalized to ^{130}Xe and to the isotopic composition of the modern atmosphere (Ozima and Podosek, 2002) ($\delta^{i}Xe_{air} = 0$ ‰): $\delta^{i}Xe_{air} = 1000 \times \left(\frac{(^{i}Xe/^{130}Xe)\ sample}{(^{i}Xe/^{130}Xe)\ air} - 1 \right)$. Errors at 1σ.

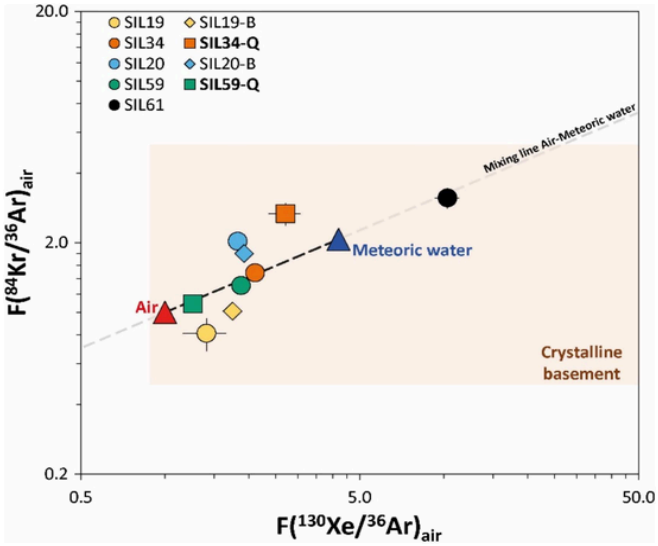

Fig. 10. Noble gas fractionation along the Siljan impact structure. The $^{84}Kr/^{36}Ar$ versus $^{130}Xe/^{36}Ar$ values are expressed as fractionation values such that Air has F = 1 [e.g., $F(Ng/^{36}Ar)_{air} = [(Ng/^{36}Ar)_{sample}/(Ng/^{36}Ar)_{air}$; Ng = ^{130}Xe or ^{84}Kr]. The red triangle represents the modern atmospheric composition, the meteoric water composition is shown as blue triangle, and the orange area shows the possible composition range of the crystalline basement (Drescher et al., 1998; Kendrick and Burnard, 2013; Ozima and Podosek, 2002). (For interpretation of the references to colour in this figure legend, the reader is referred to the web version of this article.)

incorporated during post-impact hydrothermal circulations (see section 2.1 '***Geological setting***'). Thus, elemental abundances and isotopic compositions from Siljan samples highlight a signature more complex than a simple entrapment of atmospheric noble gases during the post-hydrothermal activity induced by the impact event.

4.2.1. Crustal contamination

$^{20}Ne/^{22}Ne$ ratios from each crushing step and the total gas released during experiments for each Siljan's sample are close but lower than the present-day isotopic composition of atmospheric neon. They plot in the

lower right region of the figure, corresponding to high $^{21}Ne/^{22}Ne$ and low $^{20}Ne/^{22}Ne$ ratios, signing the presence of nucleogenic neon produced in the Earth's crustal rocks (Kennedy et al., 1990). Nevertheless, Siljan data are slightly lower than the typical Air-nucleogenic mixing lines (Fig.5). This trend could be explained by an excess of nucleogenic ^{22}Ne produced by the $^{19}F(\alpha,n)^{22}Na(\beta^+)^{22}Ne$ reaction. Indeed, in the continental crust, the radioactive decay of $^{235,238}U$ and ^{232}Th produces α-particles, which react with surrounding nuclei, such as ^{18}O and ^{19}F isotopes to produce nucleogenic ^{21}Ne and ^{22}Ne, respectively (Wetherill, 1954). The nucleogenic $^{20}Ne/^{22}Ne$ and $^{21}Ne/^{22}Ne$ production ratios mainly depend on the O/F ratios of mineral phases located where α-particles are produced, and variable O/F ratios will change the slope of the mixing lines between the atmosphere endmember and the nucleogenic endmember in the $^{20}Ne/^{22}Ne$ versus $^{21}Ne/^{22}Ne$ space (Fig.5). Hence, the smaller the x-axis ($^{21}Ne/^{22}Ne$ values) intercept value of the lines is, the more dominant is the nucleogenic pathway producing ^{22}Ne. An excess of nucleogenic ^{22}Ne relative to atmospheric neon was observed in different studies (e.g., Bourdet et al., 2023; Drescher et al., 1998; Landis and Hofstra, 2012; Schäfer et al., 2002), and was associated to the presence of a U- and/or Th-bearing, F-rich, O-poor minerals, such as fluorite (e.g., Ballentine and Burnard, 2002; Chavrit et al., 2019), micas, and/or amphibole (Kennedy et al., 1990). Moreover, it's important to note that α-particles within rock materials have a penetration depth limited to 10–40 μm (Ziegler, 1977). Consequently, the contribution of U—Th and the target nuclides of F—O to the neon isotopes in fluid inclusions can only occur if they are either present within the fluid inclusion itself, or located within a few micrometers' proximity to the fluid inclusions, or if the fluid is already carrying nucleogenic neon produced by another source (Bourdet et al., 2023; Kennedy et al., 1990). These reactions are common in the crust, so the origin of the nucleogenic ^{22}Ne detected in the Siljan samples could be very likely due to the contamination by crustal fluids. Also, biotite and hornblende minerals are present in bulk samples measured in the present study and could also be present as micro inclusions in the quartz lattice. The presence of fluorite and apatite minerals was also noticed by Hode et al. (2003). These minerals could be responsible for the excess of nucleogenic ^{22}Ne observed in the analyzed samples. Furthermore, for mica and amphibole minerals, neutron-induced reactions such as $^{25}Mg(n,\alpha)^{22}Ne^*$ can become significant, as neutrons produced by reactions like $^{19}F(\alpha,n)^{22}Na(\beta^+)^{22}Ne^*$ and other (α,n) reactions involving elements such as Al, Si, Mg, and Fe can also contribute to the reaction $^{25}Mg(n,\alpha)^{22}Ne^*$ (Leya and Wieler, 1999; Ozima and Podosek, 2002; Yatsevich and Honda, 1997). Therefore, for these minerals, the α-particles source does not necessarily need to be near the mineral, as neutrons have significantly larger travel distances (e.g., Srámek et al., 2017).

$^{40}Ar/^{36}Ar$ ratios for argon released during each crushing step are elevated relative to the modern atmospheric ratio of 298.56 (Lee et al., 2006), and could be due to the contamination by crustal fluids and/or explained by addition of $^{40}Ar^*$ produced in situ by the radioactive decay of ^{40}K contained in the K-bearing minerals predominantly present in the samples (such as K-feldspar, mica, and/or amphibole). Indeed, the granitic samples analyzed in this study contain approximately 30–50 % alkali feldspar (albite and orthoclase), 15–30 % plagioclase (oligoclase to andesine), 25–40 % quartz, < 1–8 % biotite and/or hornblende, and show a potassium content for the bulk chemical composition of around 4 wt% (Komor and Valley, 1990). Furthermore, Herrmann et al. (2021) studied the K—Ar system in biotite and amphibole minerals from Siljan. They concluded that the impact event did not significantly affect the K—Ar system since the samples studied kept their radiogenic ^{40}Ar accumulated since their formation (ca. 1.7–1.9 Ga, Herrmann et al., 2021). However, the hydrothermal activity inside the central uplift of the Siljan structure induced a significant alteration of the biotite minerals and a partial loss of $^{40}Ar^*$, which was not observed on the amphibole minerals. Herrmann et al. (2021) explained this effect by the temperature of the hydrothermal system inside the central area reaching 200–340 °C, close to the closure temperature of the biotite but lower than the closure temperature of the amphibole. Nevertheless, this study did not show the complete resetting of the K—Ar system of the minerals present at Siljan implying that some $^{40}Ar^*$ produced before the impact could be present in the investigated samples. For quartz fractions analyses (SIL34-Q and SIL59-Q) the high $^{40}Ar/^{36}Ar$ ratio cannot be explained by the addition of $^{40}Ar^*$ produced in situ by the radioactive decay of ^{40}K from the quartz minerals, because the ^{40}K content is too low in quartz (also observed in Avice et al., 2017). This demonstrates that fluids trapped in the quartz samples do not correspond directly to meteoric water equilibrated with the atmosphere. The high $^{40}Ar/^{36}Ar$ ratio observed could be attributed to the presence of micro-inclusions of K-feldspar, biotite, and/or hornblende in the quartz lattice.

The results on the Kr isotopes show a slight enrichment in ^{86}Kr compared to the atmospheric values, and could be explained by the ^{238}U fission contribution. In addition, for xenon, $^{124\text{-}129}Xe/^{130}Xe$ ratios are air-like but excesses in $^{131\text{-}136}Xe$ isotopes are present due to spontaneous fission of ^{238}U (Fig.11). Indeed, a range of noble gas isotopes are produced in the crust by radioactive decay of U, Th, and K (^4He and $^{40}Ar^*$), U fission ($^{136}Xe^*$, $^{134}Xe^*$, $^{132}Xe^*$, $^{131}Xe^*$, and $^{86}Kr^*$), and α–or n-reactions (including $^{21}Ne^*$ and $^{22}Ne^*$) (Kendrick and Burnard, 2013). As shown in Fig. 11, the three-isotope plot involving ^{130}Xe, ^{134}Xe, and ^{136}Xe displays a two-component mixture between modern atmosphere and a ^{238}U fission component. Indeed, relative excesses of ^{134}Xe and ^{136}Xe measured in Siljan samples match the fissiogenic $^{134}Xe/^{136}Xe$ ratio for the spontaneous fission of ^{238}U ($^{134}Xe/^{136}Xe = 0.832 \pm 0.012$, Ozima and Podosek, 2002; Porcelli and Ballentine, 2002). Furthermore, the fine-grained samples, SIL19 and SIL20, show a higher contribution from the ^{238}U fission component compared to the other samples, which present a higher atmospheric signature. This stronger contribution from the ^{238}U fission component could be attributed to a relatively high con-

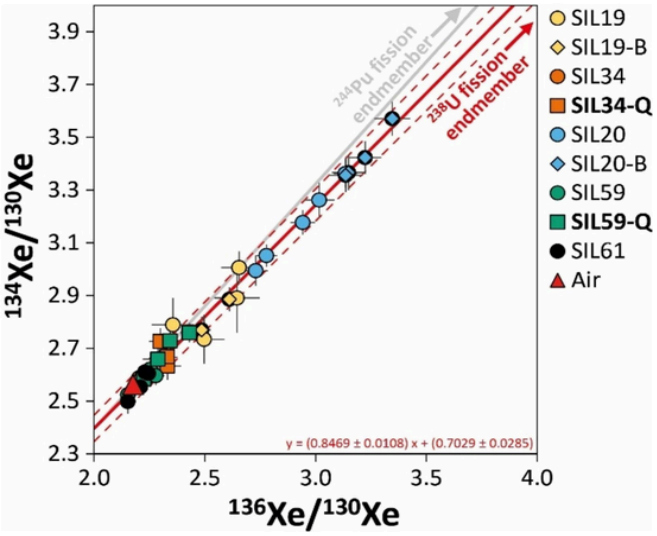

Fig. 11. Three-isotope plot of Xe for crushing experiments on Siljan samples (see data in Supp. Table 1). According to the slope of the linear regression on the results obtained on Siljan samples, data plot along the mixing line (red line) between air and the pure ^{238}U fission endmembers (Porcelli and Ballentine, 2002), not on the mixing line (grey line) between air and the pure ^{244}Pu fission endmembers. The slope defined by the data from Siljan (0.847 ± 0.011) matches the $^{134}Xe/^{136}Xe$ ratio produced by the fission of the ^{238}U (0.832 ± 0.012, Ozima and Podosek, 2002; Porcelli and Ballentine, 2002). The dashed lines represent the uncertainty at 1σ of the mixing line. (For interpretation of the references to colour in this figure legend, the reader is referred to the web version of this article.)

tribution from the crustal basement and/or accumulation of fissiogenic xenon prior to the impact, which was not completely lost.

As already noticed for neon and argon, an interaction with the crustal rocks is also clearly observed for xenon and krypton data. Indeed, the elemental graphics in **Figs. 4** and **10** show noble gas abundance ratios intermediate between meteoric water and air values, but some samples show deviation from this trend. We can observe an enrichment in $F(^{84}Kr/^{36}Ar)_{air}$ and $F(^{130}Xe/^{36}Ar)_{air}$ for SIL61, an enrichment in $F(^{84}Kr/^{36}Ar)_{air}$ is also observed for SIL20 and SIL34-Q, a depletion in $F(^{84}Kr/^{36}Ar)_{air}$ is detected for SIL19, and an enrichment in $F(^{20}Ne/^{36}Ar)_{air}$ is noted for SIL19, SIL59, and SIL59-Q. As explained above, incorporation of noble gases from crustal rocks, which typically have $^{40}Ar/^{36}Ar$ above the atmospheric value, could account for the presence of excess $^{40}Ar^*$, the range of fluid inclusion $^{84}Kr/^{36}Ar$ and $^{130}Xe/^{36}Ar$, and the presence of nucleogenic neon (Fig.12; e.g., Kendrick et al., 2006; Scarsi, 2000; Villa, 2001).

4.2.2. Contribution from older fluid inclusions

In the Siljan area, Komor et al. (1988) identified two distinct fluid-inclusion populations at different depths, characterized by their trapping temperatures, which point to the complex geological history of the impact structure (see section 1. '**Introduction**'). The validity of this hypothesis was confirmed by several studies conducted inside and outside the impact structure. These studies highlighted major events of fracturing and/or reactivation of fractures associated with hydrothermal mineralization, showing fluid inclusions with trapping temperatures below 250 °C (e.g., Sandström and Tullborg, 2009; Tillberg et al., 2021). Additionally, hydrothermal activity within the central uplift induced intense chloritization of biotite, correlating to hydrothermal system temperatures reaching 200–340 °C (Herrmann et al., 2021). Hence, at least two major hydrothermal systems have been active at Siljan: a deep system, which has been active during the cooling of the Dala granites and complexified and/or potentially reactivated by tectonic activities correlated with the geological history of the Fennoscandian shield (1.8 Ga to 440 Ma, Tillberg et al., 2021), and a shallow Devonian system within the impact structure (380 Ma) driven by heat from the impact (Herrmann et al., 2021; Komor et al., 1988). Consequently, the fluid inclusions formed before the impact could be one of the sources of the elevated $^{40}Ar/^{36}Ar$ ratios observed in the investigated samples. An alternative source for these anomalies could be fluids enriched in radiogenic ^{40}Ar trapped in microfractures and lattice defects. The excesses in ^{86}Kr and heavy Xe isotopes, due to spontaneous fission of ^{238}U fission component, could also be related to the contribution of these old fluid inclusions potentially enriched in fissiogenic Kr and Xe isotopes. Overall, while a contribution from atmosphere-derived noble gases has been clearly detected, our results do not allow to determine whether the atmospheric signal was incorporated into the studied samples as a result of the impact or if it reflects simple atmospheric contamination, which is ubiquitous in geological samples.

4.2.3. Other limits

Stepwise crushing experiments aim to progressively reduce the sample grain size under high vacuum, which allow to open vesicles and fluid inclusions in a given sample (e.g., Avice et al., 2018; Burnard et al., 2013; Kendrick and Phillips, 2009; Saito et al., 2018; Scarsi, 2000; Xiao et al., 2022). However, this technique can release simultaneously gases from different sources, such as primary and secondary fluid inclusions, impurities as well as micro-cracks and lattice, especially when prolonged crushing process is used (Kendrick et al., 2006; Scarsi, 2000; Villa, 2001). Furthermore, lattice-hosted noble gases are preferentially released by prolonged in vacuo crushing in the order Ar > Kr > Xe (Kendrick and Phillips, 2009). All these studies confirm that stepwise crushing under high vacuum can be used to selectively analyze fluid inclusions, but also indicate that the duration of crushing experiments need to be taken into account in order to understand the source of the gases released. In the case of Siljan, the $^{40}Ar^*$ measured could be a mixture of gas released from fluid inclusions and from the lattice of K-bearing minerals. Indeed, our data show an increase of the $^{40}Ar/^{36}Ar$ ratio with the number of crushing steps, and the last steps with a number of crushes between 100 and 300 strokes show higher ratios than the first steps with 10 to 50 strokes applied (**Supp. Table 1**).

Also, the low amounts of noble gases released during our experiments could introduce some uncertainty. Indeed, noble gases abundances from the standard is 2 to 20 times higher than gases released from the Siljan samples. For krypton, a depletion on light isotopes can be observed (^{82}Kr, ^{83}Kr). Fig. 13 shows a slight mass-dependent fractionation for the Siljan samples and could be due to a mismatch between standard and sample gas amounts introduced into the mass spectrometer. This deviation is usually corrected by the systematic measurement of a standard, but the low abundances of noble gases from Siljan samples could make this correction less efficient. Furthermore, $^{78}Kr/^{84}Kr$ ratios are dispersed around the air values and show high uncertainty compared to the other krypton isotopic ratios. The ^{78}Kr is the lightest isotope of krypton with an isotopic abundance of 0.35 % for air (Ozima and Podosek, 2002). Similarly, the ^{124}Xe and ^{126}Xe are the lightest isotopes of xenon with an isotopic abundance of 0.095 % and 0.089 % for air, respectively (Ozima and Podosek, 2002). The large uncertainty and dispersion observed in this study could be attributed to the relatively low abundance of these isotopes.

In addition, the fine-grained samples (SIL19 and SIL20) show higher $^{40}Ar/^{36}Ar$ ratios than coarse-grained samples (SIL34, SIL59, and SIL61). That could be attributed to the possibility that more K-bearing minerals (e.g., K-feldspars, biotite, hornblende) were present in the fine-grained samples due to the difficulty to manually select "pure" phases. Simi-

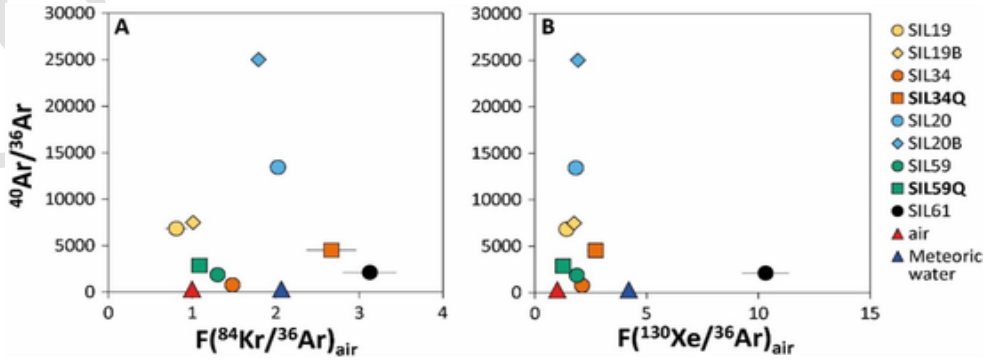

Fig. 12. Noble gas data of Siljan samples. $^{40}Ar/^{36}Ar$ is not correlated with $F(^{84}Kr/^{36}Ar)_{air}$ (A) and $F(^{130}Xe/^{36}Ar)_{air}$ (B) indicating that the data cannot be simply explained only by the presence of modern air contamination.

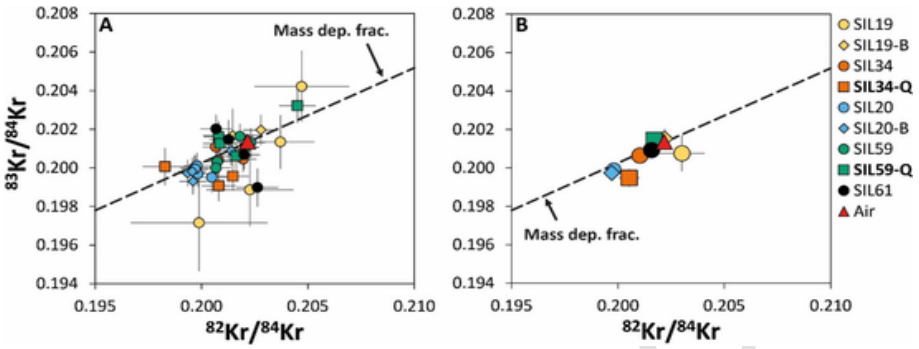

Fig. 13. Three-isotope diagram of krypton for each crushing experiment on Siljan samples (see data in Supp. Table 1). These graphics show the results for (A) each crushing step, and (B) the total gas released during the experiment of each sample. The red triangle represents the atmosphere composition. The dashed line corresponds to the mass-dependent fractionation curve (based on $m^{1/2}$). (For interpretation of the references to colour in this figure legend, the reader is referred to the web version of this article.)

larly, the fine-grained samples, SIL19 and SIL20, show a higher contribution from the ^{238}U fission component compared to the other samples which present a higher atmospheric signature. This stronger contribution from the ^{238}U fission component could be attributed to a high contribution from the crustal basement (U-bearing minerals) and/or a higher amounts of fluid inclusions than other samples analyzed in this study.

Consequently, these various processes induce difficulties to the definition of the exact sources of nucleogenic ^{22}Ne, radiogenic ^{40}Ar, and fissiogenic Kr and Xe observed in the investigated samples from Siljan.

4.3. PDFs contribution

Unfortunately, in this study, PDF-rich samples (such as SIL61) do not show higher abundances of atmospheric gases compared to samples that are devoid of PDFs (such as SIL34). This could be due to crustal contamination signature masking the atmospheric signal.

Nevertheless, we notice that quartz fractions show higher $^{21}Ne/^{22}Ne$ ratios compared to whole rocks results. This could be attributed to the fact that nucleogenic neon could be carried by the fluid present in fluid inclusions, which are common features of the quartz samples. Also, the abundances of noble gases in quartz fractions are relatively low compared to the whole rock analyses (especially in SIL34-Q), and the uncertainty could be higher in quartz fractions analyses.

Furthermore, two different quartz fractions were analyzed: SIL59-Q, sampled at 7 km from the center of the impact structure, presenting strong shocked-induced effects in minerals (10–15 GPa, Holm et al., 2011), and decorated PDFs; and SIL34-Q, collected at 10 km from the center where the recorded shock pressure (2–5 GPa, Holm et al., 2011) is below the pressure level at which PDFs start to form, i.e., 5–8 GPa (e.g., Grieve et al., 1996). The results from these two quartz fractions show some differences that could be attributed to the presence of PDFs. Indeed, quartz fraction from SIL59-Q, rich in PDFs, shows: i) A higher elemental abundance released during the experiments, inducing that more gases were contained in this fraction compared to SIL34-Q; ii) A lower $^{20}Ne/^{22}Ne$ ratio compared to SIL34-Q, and a triple neon isotope composition which plots along a nucleogenic production line with a $^{21}Ne/^{22}Ne$ ratio of 0.2 for a $^{20}Ne/^{22}Ne = 0$; iii) A higher abundance of ^{36}Ar inducing a lower $^{40}Ar/^{36}Ar$ ratio compared to SIL34-Q; iv) Isotopic compositions in Kr and Xe closer to the atmospheric values; v) F values are closer to atmospheric value compared to SIL34-Q, which shows clear interaction with the crustal basement (Fig.10). These observations highlight that shocked quartz with decorated PDFs present stronger atmospheric signature according to the results obtained for argon, krypton, and xenon. The data obtained for SIL59-Q on neon show a higher nucleogenic contribution, and could be attributed to the presence of more impurities rich in F compared to SIL34-Q. Indeed, the quartz minerals selected from SIL59 and inspected under a binocular microscope show more mineral inclusions like biotite than the quartz fraction from SIL34. This trend shows the potential of PDF-rich quartz to preserve atmospheric signal, but more investigations are necessary to confirm if shocked quartz grains could be a good paleo-atmospheric proxy.

5. Conclusion

In this study, we aimed at exploring if rocks that have been subjected to shock metamorphism, and in which decorated planar deformation features in quartz grains occur, make good paleo-atmospheric proxies. We measured the elemental abundances and isotopic composition of noble gases contained in previously studied shocked granitic and volcanic samples from the Siljan impact structure (Holm et al., 2011; Holm-Alwmark et al., 2017). Crushing results reveal the presence of noble gases derived from the atmosphere probably located in fluid inclusions and/or in the interstitial space between crystals. These atmospheric gases are accompanied by crustal-derived nucleogenic, radiogenic, and fissiogenic noble gas isotopes. Indeed, Siljan data are roughly distributed between air and meteoric water noble gas elemental abundances values, which suggests that some atmospheric signal has been incorporated (confirmed by both Kr and Xe data). However, the presence of $^{40}Ar^*$, fissiogenic Kr and Xe, and nucleogenic Ne highlight the interaction with crustal rocks during the hydrothermal circulation after the impact. Furthermore, the whole rock analyses of PDF-rich samples do not show significantly more gas or a stronger atmospheric signal compared to samples in which PDFs in quartz are less abundant and/or absent. However, results obtained on the two separated quartz fractions highlight stronger atmospheric signature correlated with the presence of PDFs. The Siljan samples investigated in this study present some issues to be considered as good paleo-atmospheric proxies, such as: i) Low amounts of gas released during the experiments, leading to relatively poor precisions for the measurements; ii) Interactions between hydrothermal fluids and the crustal basement inducing excesses in nucleogenic, radiogenic, and fissiogenic noble gas isotopes. Additionally, impurities in minerals contribute to the noble gas isotopic and elemental composition signature of the Siljan samples; iii) The difficulties to select pure quartz minerals in Siljan samples leading to a lack of observation of the PDFs contribution; iv) Multiple generations of fluids identified from our measurements and reflecting contributions from distinct hydrothermal events (during the cooling of the Dala granites, during the geological history of the Fennoscandian shield, and after the impact event).

Because a number of impacts on Earth are relatively well dated, and their associated post-impact hydrothermal systems are relatively short-

lived, rocks from impact craters remain promising paleo-atmospheric archives. Samples containing fluid inclusions with decorated PDFs, like the ones analyzed in the present study, do not seem to show a strong atmospheric signal. More importantly, they also carry inherited signatures from older crustal fluids (this study). The potential of PDFs-carrying samples to trap the composition of the Earth's atmosphere around the time of a meteorite impact could be further investigated by studying samples from other impact craters, with a careful selection of pristine unshocked samples, for a better comparison of the noble gas content and isotopic composition of shocked and unshocked lithologies. Target rocks originally poor in volatile elements (e.g., relatively unfractured granitoids) are preferable to limit the contribution from ancient crustal fluids to the potentially trapped atmospheric component. For the reasons mentioned above, future paleo-atmospheric studies using impact-related samples should prioritize samples from well-characterized and, if possible, well-dated post-impact hydrothermal systems (see Avice et al., 2023). For example, some samples, such as nodular agate samples located in cavities present in impact melt sheets (e.g., Kinnunen and Lindqvist, 1998) are promising because they clearly result from the post-impact hydrothermal system. In this context, impact structures with a clear mineral paragenesis typical of post-impact hydrothermal activity and the absence of later fluid circulations, which could have reset the trapped atmospheric signal, should be prioritized.

Supplementary data to this article can be found online at https://doi.org/10.1016/j.chemgeo.2024.122440.

CRediT authorship contribution statement

Fanny Cattani: Writing – original draft, Validation, Investigation, Formal analysis. **Guillaume Avice:** Writing – review & editing, Validation, Supervision, Methodology, Investigation, Funding acquisition, Conceptualization. **Ludovic Ferriere:** Writing – review & editing, Resources. **Sanna Alwmark:** Writing – review & editing, Resources.

Declaration of competing interest

The authors declare that they have no known competing financial interests or personal relationships that could have appeared to influence the work reported in this paper.

Acknowledgments

The authors thank the Institut de physique du globe de Paris (IPGP), and the Centre National de la Recherche Scientifique (CNRS) for their financial support. This project has received funding from DIM Origines (Région Ile-de-France) for F. Cattani post-doctoral fellowship, from the Agence Nationale de la Recherche (ANR) via the AAP T-ERC StG ATTRACTE, and from the European Research Council (ERC) under the European Union's Horizon Europe research and innovation program (grant agreement no. 101041122 to G. Avice). S. Alwmark acknowledges funding from the Swedish Research Council (Vetenskapsrådet, VR), grant # 2022-04255. We thank Sujoy Mukhopadhyay and Samuel Niedermann for their constructive reviews that improved the manuscript. We thank Don Porcelli for the editorial handling of this manuscript.

Data availability

The data used in this manuscript are available through IPGP Research Collection (research-collection.ipgp.fr) at the following DOI: 10.18715/IPGP.2024.lsekhy2p.

References

Abramov, O., Kring, D.A., 2007. Numerical modeling of impact-induced hydrothermal activity at the Chicxulub crater. Meteorit. Planet. Sci. 42, 93–112. https://doi.org/10.1111/j.1945-5100.2007.tb00220.x.

Almayrac, M.G., Broadley, M.W., Bekaert, D.V., Hofmann, A., Marty, B., 2021. Possible discontinuous evolution of atmospheric xenon suggested by Archean barites. Chem. Geol. 581, 120405. https://doi.org/10.1016/J.CHEMGEO.2021.120405.

Ames, D.E., Watkinson, D.H., Parrish, R.R., 1998. Dating of a regional hydrothermal system induced by the 1850 Ma Sudbury impact event. Geology 26, 447–450. https://doi.org/10.1130/0091-7613(1998)026<0447:DOARHS>2.3.CO;2.

Avice, G., Marty, B., Burgess, R., 2017. The origin and degassing history of the Earth's atmosphere revealed by Archean xenon. Nat. Commun. 8, 15455. https://doi.org/10.1038/ncomms15455.

Avice, G., Marty, B., Burgess, R., Hofmann, A., Philippot, P., Zahnle, K., Zakharov, D., 2018. Evolution of atmospheric xenon and other noble gases inferred from Archean to Paleoproterozoic rocks. Geochim. Cosmochim. Acta 232, 82–100. https://doi.org/10.1016/J.GCA.2018.04.018.

Avice, G., Kendrick, M.A., Richard, A., Ferrière, L., 2023. Ancient atmospheric noble gases preserved in post-impact hydrothermal minerals of the 200 Ma-old Rochechouart impact structure, France. Earth Planet. Sci. Lett. 620. https://doi.org/10.1016/j.epsl.2023.118351.

Ballentine, C.J., Burnard, P.G., 2002. Production, Release and Transport of Noble gases in the Continental Crust. Rev. Mineral. Geochem. 47, 481–538. https://doi.org/10.2138/RMG.2002.47.12.

Bekaert, D.V., Avice, G., Marty, B., Henderson, B., Gudipati, M.S., 2017. Stepwise heating of lunar anorthosites 60025, 60215, 65315 possibly reveals an indigenous noble gas component on the Moon. Geochim. Cosmochim. Acta 218, 114–131. https://doi.org/10.1016/J.GCA.2017.08.041.

Bekaert, D.V., Broadley, M.W., Delarue, F., Avice, G., Robert, F., Marty, B., 2018. Archean kerogen as a new tracer of atmospheric evolution: Implications for dating the widespread nature of early life. Sci. Adv. 4. https://doi.org/10.1126/SCIADV.AAR2091.

Bingen, B., Skår, Ø., Marker, M., Sigmond, E.M.O., Nordgulen, Ø., Ragnhildstveit, J., Mansfeld, J., Tucker, R.D., Liégeois, J.-P., 2005. Timing of continental building in the Sveconorwegian orogen, SW Scandinavia. Nor. J. Geol. 85, 87–116. https://doi.org/10.1007/s00531-007-0281-0.

Blamey, N.J.F., Brand, U., Parnell, J., Spear, N., Lécuyer, C., Benison, K., Meng, F., Ni, P., 2016. Paradigm shift in determining Neoproterozoic atmospheric oxygen. Geology 44, 651–654. https://doi.org/10.1130/G37937.1.

Bourdet, J., Piane, C.D., Wilske, C., Mallants, D., Suckow, A., Questiaux, D., Gerber, C., Crane, P., Deslandes, A., Martin, L., Aleshin, M., 2023. Natural hydrogen in low temperature geofluids in a Precambrian granite, South Australia. Implications for hydrogen generation and movement in the upper crust. Chem. Geol. 638, 121698. https://doi.org/10.1016/J.CHEMGEO.2023.121698.

Brander, L., Söderlund, U., 2009. Mesoproterozoic (1.47-1.44 Ga) orogenic magmatism in Fennoscandia; Baddeleyite U-Pb dating of a suite of massif-type anorthosite in S. Sweden. Int. J. Earth Sci. 98, 499–516. https://doi.org/10.1007/s00531-007-0281-0.

Broadley, M.W., Bekaert, D.V., 2024. Noble gas mass spectrometry. In: Reference Module in Earth Systems and Environmental Sciences. Elsevier. https://doi.org/10.1016/B978-0-323-99762-1.00097-8.

Burnard, P., 2013. The noble gases as geochemical tracers. In: The Noble Gases as Geochemical Tracers. Springer Berlin Heidelberg. https://doi.org/10.1007/978-3-642-28836-4.

Burnard, P., Zimmermann, L., Sano, Y., 2013. The noble gases as geochemical tracers: History and background. In: Advances in Isotope Geochemistry. Springer, pp. 1–15. https://doi.org/10.1007/978-3-642-28836-4_1.

Catling, D.C., Kasting, J.F., 2017. Atmospheric Evolution on Inhabited and Lifeless Worlds. Cambridge University Press. https://doi.org/10.1017/9781139020558.

Catling, D.C., Zahnle, K.J., 2020. The Archean atmosphere. Sci. Adv. 6, eaax1420. https://doi.org/10.1126/sciadv.aax1420.

Chavrit, D., Moreira, M.A., Fike, D.A., Moynier, F., 2019. Unusual neon isotopic composition in Neoproterozoic sedimentary rocks: Fluorine bearing mineral contribution or trace of an impact event? Chem. Geol. 520, 52–59. https://doi.org/10.1016/J.CHEMGEO.2019.04.025.

Corfu, F., Gasser, D., Chew, D.M., 2014. New perspectives on the Caledonides of Scandinavia and related areas: introduction. Geol. Soc. Lond. Spec. Publ. 390, 1–8. https://doi.org/10.1144/SP390.28.

Drake, H., Roberts, N.M.W., Heim, C., Whitehouse, M.J., Siljeström, S., Kooijman, E., Broman, C., Ivarsson, M., Åström, M.E., 2019. Timing and origin of natural gas accumulation in the Siljan impact structure, Sweden. Nat. Commun. 10, 4736. https://doi.org/10.1038/s41467-019-12728-y.

Drescher, J., Kirsten, T., Schäfer, K., 1998. The rare gas inventory of the continental crust, recovered by the KTB Continental Deep Drilling Project. Earth Planet. Sci. Lett. 154, 247–263. https://doi.org/10.1016/S0012-821X(97)00185-4.

Eberhardt, P., Eugster, O., Marti, K., 1965. A redetermination of the isotopic composition of atmospheric neon. Zeitschrift fur Naturfors. - Sect. A J. Phys. Sci. 20, 623–624. https://doi.org/10.1515/ZNA-1965-0420/MACHINEREADABLECITATION/RIS.

Ehlmann, B.L., Anderson, F.S., Andrews-Hanna, J., Catling, D.C., Christensen, P.R., Cohen, B.A., Dressing, C.D., Edwards, C.S., Elkins-Tanton, L.T., Farley, K.A., Fassett, C.I., Fischer, W.W., Fraeman, A.A., Golombek, M.P., Hamilton, V.E., Hayes, A.G., Herd, C.D.K., Horgan, B., Hu, R., Jakosky, B.M., Johnson, J.R., Kasting, J.F., Kerber, L., Kinch, K.M., Kite, E.S., Knutson, H.A., Lunine, J.I., Mahaffy, P.R., Mangold, N., McCubbin, F.M., Mustard, J.F., Niles, P.B., Quantin-Nataf, C., Rice, M.S., Stack, K.M., Stevenson, D.J., Stewart, S.T., Toplis, M.J., Usui, T., Weiss, B.P., Werner, S.C.,

Wordsworth, R.D., Wray, J.J., Yingst, R.A., Yung, Y.L., Zahnle, K.J., 2016. The sustainability of habitability on terrestrial planets: Insights, questions, and needed measurements from Mars for understanding the evolution of Earth-like worlds. J. Geophys. Res. Planet. 121, 1927–1961. https://doi.org/10.1002/2016JE005134.

Ferrière, L., Raiskila, S., Osinski, G.R., Pesonen, L.J., Lehtinen, M., 2010. The Keurusselkä impact structure, Finland—Impact origin confirmed by characterization of planar deformation features in quartz grains. Meteorit. Planet. Sci. 45, 434–446. https://doi.org/10.1111/J.1945-5100.2010.01032.X.

Fredriksson, K., Wickman, F.E., 1963. Meteoriter. Svensk Naturvetenskap 16, 121–157.

Goltrant, O., Leroux, H., Doukhan, J.C., Cordier, P., 1992. Formation mechanisms of planar deformation features in naturally shocked quartz. Phys. Earth Planet. Inter. 74, 219–240. https://doi.org/10.1016/0031-9201(92)90012-K.

Grieve, R.A.F., 1982. The record of impact on Earth: Implications for a major cretaceous/Tertiary impact event. In: Silver, L.T., Schultz, P.H. (Eds.), Geological Implications of Impacts of Large Asteroids and Comets on the Earth. Geological Society of America, Inc, Boulder, Colorado, pp. 25–37. https://doi.org/10.1130/SPE190-p25.

Grieve, R.A.F., 1988. The formation of large impact structures and constraints on the nature of Siljan. In: Bodén, A., Eriksson, K.G. (Eds.), Deep Drilling in Crystalline Bedrock Volume 1. The Deep gas Drilling in the Siljan Impact Structure, Sweden and Astroblemes. Springer Verlag, Berlin, pp. 328–348.

Grieve, R.A.F., Langenhorst, F., Stöffler, D., 1996. Shock metamorphism of quartz in nature and experiment: II. Significance in geoscience*. Meteorit. Planet. Sci. 31, 6–35. https://doi.org/10.1111/J.1945-5100.1996.TB02049.X.

Henkel, H., Aaro, S., 2005. Geophysical Investigations of the Siljan Impact Structure — a Short Review. Impact Tecton. 247–283. https://doi.org/10.1007/3-540-27548-7_9.

Herrmann, M., Alwmark, C., Storey, M., 2021. In: Reimold, W.U., Koeberl, C. (Eds.), 40Ar/39Ar age evidence for an impact-generated hydrothermal system in the Devonian Siljan crater, Sweden. Large Meteorite Impacts and Planetary Evolution VI. GSA Special Paper, pp. 569–583. https://doi.org/10.1130/2021.2550(26).

Hode, T., Von Dalwigk, I., Broman, C., 2003. A Hydrothermal System Associated with the Siljan Impact Structure, Sweden—Implications for the Search for Fossil Life on Mars. Astrobiology 3, 271–289. https://doi.org/10.1089/153110703769016370.

Holm, S., Alwmark, C., Alvarez, W., Schmitz, B., 2011. Shock barometry of the Siljan impact structure, Sweden. Meteorit. Planet. Sci. 46, 1888–1909. https://doi.org/10.1111/J.1945-5100.2011.01303.X.

Holm-Alwmark, S., 2021. Impact cratering record of Sweden—A review. In: Reimold, W.U., Koeberl, C. (Eds.), Large Meteorite Impacts and Planetary Evolution VI. Geological Society of America, pp. 1–39. https://doi.org/10.1130/2021.2550(01).

Holm-Alwmark, S., Rae, A.S.P., Ferrière, L., Alwmark, C., Collins, G.S., 2017. Combining shock barometry with numerical modeling: Insights into complex crater formation—the example of the Siljan impact structure (Sweden). Meteorit. Planet. Sci. 52, 2521–2549. https://doi.org/10.1111/MAPS.12955.

Holm-Alwmark, S., Erickson, T.M., Cavosie, A.J., 2022. Empirical constraints on progressive shock metamorphism of magnetite from the Siljan impact structure, Sweden. Geology 50, 377–382. https://doi.org/10.1130/G49498.1.

Johansson, Å., 1984. Geochemical studies on the Boda pb-Zn deposit in the siljan astrobleme, Central Sweden. GFF 106, 15–25. https://doi.org/10.1080/11035898409454598.

Jourdan, F., Reimold, W.U., Deutsch, A., 2012. Dating Terrestrial Impact Structures. Elements 8, 49–53. https://doi.org/10.2113/GSELEMENTS.8.1.49.

Kendrick, M.A., Burnard, P., 2013. Noble gases and halogens in fluid inclusions: A journey through the earth's crust. In: Burnard, P. (Ed.), Advances in Isotope Geochemistry. Springer, pp. 319–369. https://doi.org/10.1007/978-3-642-28836-4_11/COVER.

Kendrick, M.A., Phillips, D., 2009. New constraints on the release of noble gases during in vacuo crushing and application to scapolite Br–Cl–I and 40Ar/39Ar age determinations. Geochim. Cosmochim. Acta 73, 5673–5692. https://doi.org/10.1016/J.GCA.2009.06.032.

Kendrick, M.A., Miller, J.M.L., Phillips, D., 2006. Part II. Evaluation of 40Ar–39Ar quartz ages: Implications for fluid inclusion retentivity and determination of initial 40Ar/36Ar values in Proterozoic samples. Geochim. Cosmochim. Acta 70, 2562–2576. https://doi.org/10.1016/J.GCA.2005.12.024.

Kenkmann, T., Hornemann, U., Stöffler, D., 2000. Experimental generation of shock-induced pseudotachylites along lithological interfaces. Meteorit. Planet. Sci. 35, 1275–1290. https://doi.org/10.1111/J.1945-5100.2000.TB01516.X.

Kennedy, B.M., Lynch, M.A., Reynolds, J.H., Smith, S.P., 1985. Intensive sampling of noble gases in fluids at Yellowstone: I. Early overview of the data; regional patterns. Geochim. Cosmochim. Acta 49, 1251–1261. https://doi.org/10.1016/0016-7037(85)90014-6.

Kennedy, B.M., Hiyagon, H., Reynolds, J.H., 1990. Crustal neon: a striking uniformity. Earth Planet. Sci. Lett. 98, 277–286. https://doi.org/10.1016/0012-821X(90)90030-2.

Kinnunen, K.A., Lindqvist, K., 1998. Agate as an indicator of impact structures: an example from Sääksjärvi, Finland. Meteorit. Planet. Sci. 33, 7–12. https://doi.org/10.1111/J.1945-5100.1998.TB01603.X.

Komor, S.C., Valley, J.W., 1990. Deep drilling at the Siljan Ring impact structure: oxygen-isotope geochemistry of granite. Contrib. Mineral. Petrol. 105, 516–532. https://doi.org/10.1007/BF00302492.

Komor, S.C., Valley, J.W., Brown, P.E., 1988. Fluid-inclusion evidence for impact heating at the Siljan Ring, Sweden. Geology 16, 711–715. https://doi.org/10.1130/0091-7613(1988)016<0711:FIEFIH>2.3.CO;2.

Kring, D.A., Tikoo, S.M., Schmieder, M., Riller, U., Rebolledo-Vieyra, M., Simpson, S.L., Osinski, G.R., Gattacceca, J., Wittmann, A., Verhagen, C.M., Cockell, C.S., Coolen, L., Longstaffe, M.J.F.J., Gulick, S.P., Morgan, J.V., Bralower, T.J., Chenot, E., Christeson, G.L., Claeys, P., Ferrière, L., Gebhardt, C., Goto, K., Green, S.L., Jones, H., Lofi, J., Lowery, C.M., Ocampo-Torres, R., Perez-Cruz, L., Pickersgill, A.E., Poelchau, M.H., Rae, P., Rasmussen, A.S.C., Sato, H., Smit, J., Tomioka, N., Urrutia-Fucugauchi, J., Whalen, M.T., Xiao, L., Yamaguchi, K.E., 2020. Probing the hydrothermal system of the Chicxulub impact crater. Sci. Adv. 6. https://doi.org/10.1126/sciadv.aaz3053. . eaaz3053.

Landis, G.P., Hofstra, A.H., 2012. Ore genesis constraints on the Idaho cobalt belt from fluid inclusion gas, noble gas isotope, and ion ratio analyses. Soc. Econom. Geolo. Inc. 107, 1189–1205. https://doi.org/10.2113/ECONGEO.107.6.1189.

Lee, J.-Y., Marti, K., Severinghaus, J.P., Kawamura, K., Yoo, H.-S., Lee, J.B., Kim, J.S., 2006. A redetermination of the isotopic abundances of atmospheric Ar. Geochim. Cosmochim. Acta 70, 4507–4512. https://doi.org/10.1016/j.gca.2006.06.1563.

Leya, I., Wieler, R., 1999. Nucleogenic production of Ne isotopes in Earth's crust and upper mantle induced by alpha particles from the decay of U and Th. J. Geophys. Res. Solid Earth 104, 15439–15450. https://doi.org/10.1029/1999jb900134.

Lindblom, S., Wickman, F.E., 1985. Fluid inclusions in quartz from a quartz breccia in the Siljan Ring structure, Central Sweden. Geol. Föreningen i Stockh. Förhandling. 107, 53–58. https://doi.org/10.1080/11035898509452613.

Lippmann-Pipke, J., Sherwood Lollar, B., Niedermann, S., Stroncik, N.A., Naumann, R., van Heerden, E., Onstott, T.C., 2011. Neon identifies two billion year old fluid component in Kaapvaal Craton. Chem. Geol. 283, 287–296. https://doi.org/10.1016/J.CHEMGEO.2011.01.028.

Lundmark, A.M., Lamminen, J., 2016. The provenance and setting of the Mesoproterozoic Dala Sandstone, western Sweden, and paleogeographic implications for southwestern Fennoscandia. Precambrian Res. 275, 197–208. https://doi.org/10.1016/J.PRECAMRES.2016.01.003.

Marty, B., 2020. Origins and early evolution of the atmosphere and the oceans. Geochem. Perspect 9, 135–313. https://doi.org/10.7185/GEOCHEMPERSP.9.2.

Meshik, A., Hohenberg, C., Pravdivtseva, O., Burnett, D., 2014. Heavy noble gases in solar wind delivered by Genesis mission. Geochim. Cosmochim. Acta 127, 326–347. https://doi.org/10.1016/J.GCA.2013.11.030.

Moreira, M., Kunz, J., Allègre, C., 1998. Rare Gas Systematics in Popping Rock: Isotopic and Elemental Compositions in the Upper Mantle. Science 279, 1178–1181. https://doi.org/10.1126/science.279.5354.1178.

Naumov, M.V., 2002. Impact-Generated Hydrothermal Systems: Data from Popigai, Kara, and Puchezh-Katunki Impact Structures. In: Plado, J., Pesonen, L.J. (Eds.), Impacts in Precambrian Shields (Impact Studies). Springer-Verlag, Berlin Heidelberg, pp. 117–171. https://doi.org/10.1007/978-3-662-05010-1_6.

Naumov, M.V., 2005. Principal features of impact-generated hydrothermal circulation systems: mineralogical and geochemical evidence. Geofluids 5, 165–184. https://doi.org/10.1111/J.1468-8123.2005.00092.X.

Newsom, H.E., 1980. Hydrothermal alteration of impact melt sheets with implications for Mars. Icarus 44, 207–216. https://doi.org/10.1016/0019-1035(80)90066-4.

Newsom, H.E., Brittelle, G.E., Hibbitts, C.A., Crossey, L.J., Kudo, A.M., 1996. Impact crater lakes on Mars. J. Geophys. Res. 101, 14951–14965. https://doi.org/10.1029/96JE01139.

Newsom, H.E., Hagerty, J.J., Thorsos, I.E., 2001. Location and sampling of aqueous and hydrothermal deposits in martian impact craters. Astrobiology 1, 71–88. https://doi.org/10.1089/153110701750137459.

Osinski, G.R., Grieve, R.A.F., Ferrière, C.L., Losiak, A., Pickersgill, A.E., Cavosie, A.J., Hibbard, S.M., Hill, P.J.A., Jaimes Bermudez, J., Marion, C.L., Newman, J.D., Simpson, S.L., 2022. Impact Earth: a review of the terrestrial impact record. Earth Sci. Rev. 232, 104112. https://doi.org/10.1016/j.earscirev.2022.104112.

Ozima, M., Podosek, F.A., 2002. Noble gas Geochemistry, Second edition. Cambridge University Press, Cambridge. https://doi.org/10.1017/CBO9780511545986.

Porcelli, D., Ballentine, C.J., 2002. Models for distribution of Terrestrial Noble gases and Evolution of the Atmosphere. Rev. Mineral. Geochem. 47, 411–480. https://doi.org/10.2138/RMG.2002.47.11.

Pujol, M., Marty, B., Burgess, R., 2011. Chondritic-like xenon trapped in Archean rocks: a possible signature of the ancient atmosphere. Earth Planet. Sci. Lett. 308, 298–306. https://doi.org/10.1016/J.EPSL.2011.05.053.

Rondot, J., 1975. Comparaison entre les astroblemes de Siljan, Suède et de Charlevoix, Québec. Bull. Geol. Institut. Univer. Uppsala 6, 85–92.

Saito, T., Qiu, H.N., Shibuya, T., Li, Y.B., Kitajima, K., Yamamoto, S., Ueda, H., Komiya, T., Maruyama, S., 2018. Ar-Ar dating for hydrothermal quartz from the 2.4 Ga Ongeluk Formation, South Africa: Implications for seafloor hydrothermal circulation. R. Soc. Open Sci. 5, 180260. https://doi.org/10.1098/RSOS.180260.

Sandström, B., Tullborg, E.L., 2009. Episodic fluid migration in the Fennoscandian Shield recorded by stable isotopes, rare earth elements and fluid inclusions in fracture minerals at Forsmark, Sweden. Chem. Geol. 266, 126–142. https://doi.org/10.1016/j.chemgeo.2009.04.019.

Scarsi, P., 2000. Fractional extraction of helium by crushing of olivine and clinopyroxene phenocrysts: effects on the 3He/4He measured ratio. Geochim. Cosmochim. Acta 64, 3751–3762. https://doi.org/10.1016/S0016-7037(00)00419-1.

Schäfer, J.M., Tschudi, S., Zhao, Z., Wu, X., Ivy-Ochs, S., Wieler, R., Baur, H., Kubik, P.W., Schlüchter, C., 2002. The limited influence of glaciations in Tibet on global climate over the past 170 000 yr. Earth Planet. Sci. Lett. 194, 287–297. https://doi.org/10.1016/S0012-821X(01)00573-8.

Schmieder, M., Kring, D.A., 2020. Earth's Impact events through Geologic Time: a list of Recommended Ages for Terrestrial Impact Structures and deposits. Astrobiology 20, 91–141. https://doi.org/10.1089/AST.2019.2085/ASSET/IMAGES/LARGE/AST.2019.2085_FIGURE9.JPEG.

Short, N.M., Gold, D.P., 1996. Petrography of shocked rocks from the central peak at the Manson impact structure. In: Koeberl, C., Anderson, R.R. (Eds.), The Manson Impact Structure, Iowa; Anatomy of an Impact Crater. Geological Society of America, pp. 245–265. https://doi.org/10.1130/0–8137–2302-7.245.

Smith, S.P., Kennedy, B.M., 1983. The solubility of noble gases in water and in NaCl brine. Geochim. Cosmochim. Acta 47, 503–515. https://doi.org/10.1016/0016-7037(83)90273-9.

Srámek, O., Stevens, L., Mcdonough, W.F., Mukhopadhyay, S., Peterson, R.J., 2017. Subterranean production of neutrons, 39 Ar and 21 Ne: rates and uncertainties. Geochim. Cosmochim. Acta 196, 370–387. https://doi.org/10.1016/j.gca.2016.09.040.

Stephens, Michael B., 2020. Introduction to the lithotectonic framework of Sweden and organization of this memoir. In: Stephens, M.B., Bergman Weihed, J. (Eds.), Sweden: Lithotectonic Framework, Tectonic Evolution and Mineral Resources. Geological Society of London, pp. 1–15. https://doi.org/10.1144/M50-2019-21.

Svensson, N.B., 1971. Probable Meteorite Impact Crater in Central Sweden. Nat. Phys. Sci. 229, 90–92. https://doi.org/10.1038/physci229090a0.

Svensson, N.B., 1973. Shatter cones from the Siljan structure, Central Sweden. Geol. Förening. Stockh. Förhandlingar 95, 139–143. https://doi.org/10.1080/11035897309455436.

Tamminen, J., Wickman, F.E., 1980. Shock effects in pegmatitic quartz from the Siljan ring structure, Central Sweden. Geol. Föreningen i Stockh. Förhandling. 102, 275–278. https://doi.org/10.1080/11035898009455171.

Tillberg, M., Drake, H., Zack, T., Hogmalm, J., Kooijman, E., Åström, M., 2021. Reconstructing craton-scale tectonic events via in situ Rb-Sr geochronology of polyphased vein mineralization. Terra Nova 33, 502–510. https://doi.org/10.1111/TER.12542.

Trepmann, C.A., Spray, J.G., 2006. Shock-induced crystal-plastic deformation and post-shock annealing of quartz: microstructural evidence from crystalline target rocks of the Charlevoix impact structure, Canada. Eur. J. Mineral. 18, 161–173. https://doi.org/10.1127/0935-1221/2006/0018-0161.

Valley, J.W., Komor, S.C., Baker, K., Jeffrey, A.W., Kaplan, I.R., Raheim, A., 1988. Calcite crack cements in granite from the Siljan Ring, Sweden: Stable isotopic results. In: Bodén, A., Eriksson, K.G. (Eds.), Deep Drilling in Crystalline Bedrock Volume 1: The Deep gas Drilling in the Siljan Impact Structure, Sweden and Astroblemes. Springer Verlag, Berlin, pp. 159–179.

Villa, I.M., 2001. Radiogenic isotopes in fluid inclusions. Lithos 55, 115–124. https://doi.org/10.1016/S0024-4937(00)00041-4.

Wetherill, G.W., 1954. Variations in the Isotopic Abundances of Neon and Argon Extracted from Radioactive Minerals. Phys. Rev. 96, 679. https://doi.org/10.1103/PhysRev.96.679.

Whitehead, J., Spray, J.G., Grieve, R.A.F., 2002. Origin of "'toasted'" quartz in terrestrial impact structures. Geology 30, 431–434. https://doi.org/10.1130/0091-7613(2002)030<0431:OOTQIT>2.0.CO;2.

Wickman, F.E., Blomqvist, N.B., Geijer, P., Parwel, A., Ubisch, H., Welin, E., 1963. Isotopic constitution of ore lead in Sweden. Ark. Mineral. Geol. 3, 193–257.

Xiao, M., De Jiang, Y., Qiu, H.N., Cai, Y., Zhang, W.F., 2022. An improved gas extraction model during stepwise crushing: New perspectives on fluid geochronology and geochemistry. Ore Geol. Rev. 140, 104588. https://doi.org/10.1016/J.OREGEOREV.2021.104588.

Yatsevich, I., Honda, M., 1997. Production of nucleogenic neon in the Earth from natural radioactive decay. J. Geophys. Res. Solid Earth 102, 10291–10298. https://doi.org/10.1029/97jb00395.

Ziegler, J.F., 1977. Helium : Stopping Powers and Ranges in all Elemental Matter. Pergamon Press, New York.

Zimmermann, L., Füri, E., Burnard, P., 2015. Purification des gaz rares sous ultravide - Méthodes de purification. Techniques de l'ingénieur J6635, 1–23. https://doi.org/10.51257/A-V1-J6635.